

1

Dynamical Downscaling of Future Hydrographic Changes over the Northwest Atlantic Ocean

4 Sang-Ik Shin^{1,2,*} and Michael A. Alexander²

⁵ ¹CIRES, University of Colorado, Boulder, CO.

⁶ ²Physical Science Division, NOAA Earth System Research Laboratory, Boulder, CO.

7

Journal of Climate

9 (Submitted: July 5, 2019; Revised: November 5, 2019; Accepted: December 4, 2019)

10

* Corresponding author address: Sang-Ik Shin, NOAA/ESRL, 325 Broadway, R/PSD1, Boulder, CO 80305.

E-mail: Sangik.Shin@noaa.gov

11 **Abstract**

12 Projected climate changes along the U.S. East and Gulf Coasts were examined
13 using the eddy-resolving Regional Ocean Modeling System (ROMS). First, a control
14 (CTRL) ROMS simulation was performed using boundary conditions derived from
15 observations. Then climate change signals, obtained as mean seasonal cycle differences
16 between the recent past (1976-2005) and future (2070-2099) periods in a coupled global
17 climate model under the RCP8.5 greenhouse gas trajectory, were added to the initial and
18 boundary conditions of the CTRL in a second (RCP85) ROMS simulation. The difference
19 between the RCP85 and CTRL simulations were used to investigate the regional effects of
20 climate change.

21 Relative to the coarse resolution coupled climate model, the downscaled projection
22 shows that SST changes become more pronounced near the U.S. East Coast, and the Gulf
23 Stream is further reduced in speed and shifted southward. Moreover, the downscaled
24 projection shows enhanced warming of ocean bottom temperatures along the U.S. East and
25 Gulf Coasts, particularly in the Gulf of Maine and the Gulf of Saint Lawrence. The
26 enhanced warming was related to an improved representation of the ocean circulation,
27 including topographically trapped coastal ocean currents and slope water intrusion through
28 the Northeast Channel into the Gulf of Maine. In response to increased radiative forcing,
29 much warmer than present-day Labrador Subarctic slope waters entered the Gulf of Maine
30 through the Northeast Channel warming the deeper portions of the Gulf by more than 4°C.

31

32 **1. Introduction**

33 Projections of future ocean conditions are often requested for long term planning
34 and management of marine resources. These projections require sustained observations of
35 the system as well as a modeling framework that represents the relevant ocean processes
36 and feedbacks with other systems (e.g. atmosphere, ice, land, biogeochemistry, etc.) to
37 resolve the mechanisms important to variability of the system. In this regard, projections
38 from simulations participating in Phase 5 of the Coupled Climate Model Intercomparison
39 Project (CMIP5; Taylor et al. 2012) provide physically consistent estimates of climate
40 change over the northwest Atlantic, since those simulations include state-of-the-art ocean
41 processes and feedbacks among subsystems. However, CMIP5 models have several
42 intrinsic shortcomings, including coarse horizontal resolution, on the order of 1° in the
43 midlatitude oceans, and a limited number of vertical ocean layers. Moreover, errors in
44 coupled climate models are not uniformly distributed over the globe; for example, sea
45 surface temperature (SST) errors are generally largest along the continental margins (e.g.
46 Fig. 3 in He and Soden 2016).

47 How can we improve climate projections for coastal oceans? One approach is to
48 use a high-resolution coupled climate model. Climate models with very high resolution
49 (~10 km) in the ocean component used by Small et al. (2014), Griffies et al. (2015) and
50 Saba et al. (2016) were successful in reproducing many aspects of the ocean state and in
51 reducing biases in the coastal oceans, including the northeast U.S. coast. However, the
52 current generation of high-resolution coupled climate models still have substantial mean

53 biases. For example, the cold SST bias in the central North Atlantic remains and can exceed
54 5 °C in some high-resolution models (e.g. Fig. 2 in Saba et al. 2016).

55 Theoretical models can also be used to downscale the future coastal ocean climate.
56 Recently, Minobe et al. (2017) developed the theoretical model for sea level variability
57 along the western boundary using interior ocean sea level information and applied to assess
58 the future sea level changes between the end of the 20th and 21st centuries by using the
59 CMIP5 interior ocean information. The model successively captures the future sea level
60 rise along the western North Atlantic, qualitatively consistent with the CMIP5 multi-model
61 mean. However, such theoretical models cannot produce all necessary coastal ocean fields
62 for long term planning and management of marine resources, such as temperature, salinity
63 and ocean circulation.

64 Meanwhile, previous studies have shown that uncoupled regional ocean models,
65 employing a high-resolution grid in both horizontal and vertical directions, improve many
66 aspects of ocean processes along continental margins, including topographically trapped
67 coastal currents, eddies, tidal mixing, river plumes, etc. Regional models have been
68 especially useful in simulating ocean processes along the U.S. East Coast and Gulf of
69 Mexico (e.g. Curchitser et al. 2005; Kang and Curchitser 2013; Kang and Curchitser 2015)
70 and for shelf and bays in the Gulf of Mexico and Atlantic seaboard (Liu et al. 2012;
71 Alexander 2019), due to their complex coastlines, highly variable bathymetry, and
72 proximity to strong coastal currents. Regional ocean models can be used to investigate
73 climate change by forcing them with bias-adjusted future projections from global models.
74 This has generally been done using the “delta method”, where long-term mean differences

75 in oceanic and atmospheric fields between the recent past and future periods were derived
76 from coupled climate models, and then added to the observed present-day conditions. By
77 design, this approach only considers the effects of the long-term climate change (forced)
78 signal and neglects the somewhat uncertain future projections at higher frequencies, such
79 as changes in storm tracks and interannual climate variability.

80 Differences between low-resolution coupled and high-resolution regional models
81 are illustrated in Fig. 1, which shows the wintertime temperature and circulation patterns
82 along the northeast U.S. shelf (see Fig. S1 of Supplementary Information for the
83 summertime). The fields are obtained from the Geophysical Fluid Dynamics Laboratory
84 (GFDL) Earth System Model that includes ocean biogeochemistry, the GFDL-ESM2M
85 (Dunne et al. 2012), and 7-km Regional Ocean Modeling System (ROMS) (see section 2a
86 for details). For example, at the surface ROMS exhibits a southeastward directed coastal
87 current along Nova Scotia that flows counterclockwise around the Gulf of Maine (see the
88 schematics in Fig. 2). These currents are weak or absent in the climate model. As observed,
89 cold SSTs ($< 7^{\circ}\text{C}$) extend over the entire Gulf of Maine in ROMS, but they occur only in
90 the very northern part of the Gulf in GFDL-ESM2M. At a 155 m depth, ROMS clearly
91 shows the intrusion of slope waters into the Gulf of Maine through the Northeast Channel
92 as in observations (e.g. Brooks 1987). The slope waters are a deep-water mass, consisting
93 of Labrador Slope Water and Warm Slope Water, and recognized as the major source of
94 dissolved inorganic nutrients to the Gulf (e.g. Townsend et al. 2014; Townsend et al. 2015).
95 The Gulf of Maine, including the northeast Channel, are not resolved in GFDL-ESM2M.

96 A more detailed examination of changes in the Gulf of Maine is warranted given
97 that it has very complex bathymetry and that it is near the confluence of the cold Labrador
98 Current and warm Gulf Stream (see Fig. 2). It has also experienced very strong warming
99 over the recent past (e.g. Pershing et al. 2015) that is projected to continue into the future
100 (e.g. Saba et al. 2015). The rapidly warming temperatures and accompanying changes in
101 currents and biogeochemistry will strongly impact marine ecosystems along the northeast
102 U.S. coast, (e.g. Heogh-Guldberg and Bruno 2010), with adverse effects on species such
103 as Atlantic cod (e.g. Pershing et al. 2015) and lobster (Le Bris et al. 2017).

104 In this study, we are interested in downscaling the future coastal ocean climate
105 under the Representative Concentration Pathway (RCP) 8.5 scenario. Here, we extend the
106 previous one-way nested regional ocean model approach by retaining the “mean seasonal
107 cycle” of the delta forcing fields. Recently, Alexander et al. (2019) provided a general
108 survey of such downscaled future coastal ocean climate under the RCP 8.5 scenario using
109 three CMIP5 participating coupled climate models including the GFDL-ESM2M, and here
110 we performed a detailed analysis of the one driven by the GFDL-ESM2M. The choice of
111 GFDL-ESM2M is for the qualitative comparisons with the recent study of Saba et al.
112 (2016), where a high-resolution GFDL coupled climate model was used to assess the future
113 coastal ocean climate. The sensitivity of downscaled future climate to the choice of AR5
114 coupled climate model was given in Alexander et al. (2019). This paper is organized as
115 follows; a summary of the models and methods are given in section 2; the results of
116 downscaled ocean climate changes over the entire model domain are summarized in section
117 3; a detailed assessment of the changes in the Gulf of Maine are given in section 4; and the
118 summary and concluding remarks follow in section 5.

119

120 **2. Models and methods**

121 We first used ROMS to perform a control simulation (hereafter CTRL) of the recent
122 past along the U.S. East and Gulf Coasts. The large-scale projected changes (i.e. deltas)
123 were obtained from the GFDL-ESM2M simulations of historical and future periods. Then,
124 these delta fields were added to the initial and boundary conditions of the CTRL in a second
125 ROMS simulation (hereafter RCP85). A brief description of ROMS, the GFDL-ESM2M
126 simulations used, and delta method are given below.

127 *a. Regional ocean model*

128 Our study uses ROMS (Schepetkin and McWilliams 2005), a sigma-coordinate
129 primitive equation ocean model, with the same domain and physics as in Kang and
130 Curchitser (2013). The model domain covers the Northwest Atlantic Ocean and Gulf of
131 Mexico (hereafter NWA; see Fig. 2) with a horizontal resolution of 7 km and 40 vertical
132 terrain-following levels. For the CTRL simulation, initial and ocean lateral boundary
133 conditions (BCs) were derived from the Simple Ocean Data Assimilation (SODA; Carton
134 and Giese 2008) version 2.1.6, air-sea fluxes were calculated from the surface atmospheric
135 forcing fields extracted from the Coordinated Ocean-ice Reference Experiments (CORE)
136 version 2 data set (Large and Yeager 2009), and river discharge was implemented as a fresh
137 water flux using the global river flow and continental discharges database (Dai et al. 2009).
138 A more detailed description of the model physics is given in Kang and Curchitser (2013).

139 The CTRL was very successful in simulating many aspects of present-day climate
140 conditions over the NWA as discussed in Kang and Curchitser (2013). In Fig. 3, we
141 compared the climatological annual mean surface currents derived from the CTRL (during
142 the yrs. 1976-2005) to the satellite-tracked surface drifting buoy (during the yrs. 1979-
143 2015; Lumpkin and Johnson 2013) and the SODA data set (during the period yrs. 1976-
144 2005). Despite the difference in time averaging periods and the uncertainties of model and
145 Lagrangian drifter data, the CTRL captures the observed circulation patterns in the NWA,
146 including the observed clockwise shelf circulation in the Gulf Mexico. Such coastal
147 circulation was not resolved in the relatively low-resolution SODA reanalysis. The SODA
148 reanalysis has a horizontal resolution of about 0.25° latitude x 0.4° longitude with 40
149 vertical levels (Note that the SODA had less than 15 vertical levels at the coastal ocean
150 where depth is shallower than 200 m). The Gulf Stream in CTRL, however, shows an
151 exaggerated split into two branches over the regions between 65° - 55° W, though the drifter
152 also indicates some hints of this split. We also assessed the annual average of SSH derived
153 from aviso (<http://marine.copernicus.eu>) and the surface currents derived from OSCAR
154 (Bonjean and Lagerloef 2002) datasets. Both datasets, however, do not show the split of
155 Gulf Stream (figure not shown).

156 *b. Coupled global climate model simulations*

157 The coupled climate model simulations used in this study are the historical (yrs.
158 1976-2005) and the RCP 8.5 (yrs. 2070-2099) simulations from the GFDL-ESM2M. The
159 atmospheric component, the Atmospheric Model version 2 (AM2; Anderson et al. 2004),
160 has a horizontal resolution of 2° latitude x 2.5° longitude with 24 vertical levels. The ocean

161 component, MOM4p1 (Griffies et al. 2005), has $\sim 1^\circ$ horizontal resolution with 50 vertical
162 levels. The horizontal resolution of the ocean component decreases to $\frac{1}{3}^\circ$ meridionally at
163 the equator and uses tripolar grid north of 65°N . A detailed description of model physics is
164 given by Dunne et al. (2012).

165 The historical run is designed to simulate the recent past (yrs. 1850-2005) by
166 imposing observed radiative forcing changes due to natural (e.g. volcanoes) and
167 anthropogenic influences. The RCP 8.5 scenario, the projection with the greatest increase
168 in greenhouse gasses in CMIP5, starts in 2006 with the level of radiative forcing reaching
169 8.5 W m^{-2} by 2100. The atmospheric CO₂ rises from 354.14 ppm (average of yrs. 1976-
170 2005) to 798.51 ppm (average of yrs. 2070-2099), although other trace gases contribute to
171 the radiative forcing. The increase in radiative forcing under the RCP 8.5 scenario causes
172 the global surface temperature to rise by 2-5 °C at the end of 21st century relative to 1986-
173 2005 average depending on which climate model is used (IPCC 2013). In GFDL-ESM2M,
174 the projected change is about 4.5°C.

175 Many previous studies (e.g. Cheng et al. 2013) found that the increase in radiative
176 forcing weakens the Atlantic Meridional Overturning Circulation (AMOC). In the GFDL-
177 ESM2M model simulations, AMOC decreases by about 20 % ($\sim 4 \text{ Sv}$; $1 \text{ Sv} = 10^6 \text{ m}^3 \text{ s}^{-1}$)
178 from the current climate conditions ($\sim 20 \text{ Sv}$; figure not shown). The projected regional
179 climate changes over the North Atlantic in GFDL-ESM2M are largely consistent with the
180 climate responses to reduced AMOC. For example, a large ocean surface warming along
181 the northeast coast of the U.S that extends into the central North Atlantic and a moderate
182 warming or even a small cooling over the subpolar North Atlantic (Fig. 4a) are consistent

183 with the fingerprint pattern for reduced AMOC (e.g. Cheng et al. 2013; Buckley and
184 Marshall 2016; Caesar et al. 2018). The subtropical North Atlantic is projected to be saltier
185 than in the present-day (Fig. 4b), in contrast to the projected fresher subpolar North
186 Atlantic. These surface temperature and salinity responses are also consistent with the
187 projected slow-down of Gulf Stream (Fig. 4c) that decreases meridional oceanic heat and
188 salt transport. The ocean bottom temperatures along the East Coast of North America show
189 2-3°C year-round warming (Fig. 5), which is somewhat larger than at the surface (Fig. 4a),
190 suggesting substantial changes in ocean stratification.

191 *c. Seasonally varying delta method*

192 To produce a high-resolution, bias-adjusted future projection for the NWA, we
193 dynamically downscale the ocean climate by using the delta method to obtain initial
194 conditions and boundary conditions including the surface atmospheric fluxes. The delta
195 approach has been used previously in many coastal ocean downscaling simulations (e.g.
196 Auad et al. 2006; Liu et al. 2012; van Hooijdonk et al. 2015). In those studies, the long-term
197 (typically 10-30 year) annual mean difference in BCs and surface atmospheric forcings
198 between the recent past and future periods were derived from coupled climate models, and
199 then added to the observed present-day conditions. This method does remove the mean
200 bias for the present-day climate of the coupled climate models, but also retains high-
201 frequency spatiotemporal variability of the forcings (i.e. the day-to-day variability and fine-
202 scale spatial variability of the present-day climate). The delta method, however, neglects
203 the changes in interannual climate variability due to an increase in greenhouse gases.

204 Here we extended the delta approach by retaining its seasonal cycle, given that
205 climate change signals often show a strong seasonal dependence (Partanen et al. 2017; also
206 see our Fig. 7). The detailed procedure of estimating the seasonally varying delta is as
207 follows:

208 1) The monthly mean GFDL ESM2M simulated surface atmospheric (Table 1),
209 oceanic (sea surface height, 3-dimensional temperature, salinity, and currents), and
210 river runoff fields for 30-year periods representing the present-day (yrs. 1976-2005)
211 and future (yrs. 2070-2099; RCP 8.5) periods were obtained from the NOAA GFDL
212 CMIP5 repository.

213 2) The differences of the mean seasonal cycles between two periods were computed
214 to form the seasonally varying deltas as monthly averages.

215 3) The monthly deltas were bilinearly interpolated both in space and time, and added
216 to the SODA version 2.1.6 (pentad in time and 0.5° latitude x 0.5° longitude¹ with
217 40 vertical levels), CORE version 2 (6 hourly in time and about 1.89° in latitude
218 and longitude), and Dai et al.'s (2009) global river flow (monthly in time and 1° in
219 latitude and longitude) historical data (yrs. 1958-2005) to form a bias-corrected
220 future projection (yrs. 2052-2099).

¹ Although the SODA experiment employs a horizontal resolution of about 0.25° latitude x 0.4° longitude with 40 vertical levels, the final product was released in 0.5° latitude x 0.5° longitude horizontal grid with the same 40 vertical levels.

221 4) Then, the bias-corrected future atmospheric, oceanic, and river runoff fields were
222 interpolated to the ROMS grid by using the Pyroms package to provide the
223 boundary and initial conditions for the NWA.

224 Selected maps of the GFDL-ESM2M oceanic changes (deltas) are already shown
225 in Fig. 4 and Fig. 5 and discussed in section 2b. The maps of deltas for surface atmospheric
226 forcings and river runoff over the N. Atlantic during December-January-February (DJF)
227 and June-July-August (JJA) are shown in Fig. 6. The changes in surface atmospheric
228 forcings, by design, represent the projected future climate responses to increasing
229 greenhouse gases. For example, surface air temperature over the entire subtropical N.
230 Atlantic warms about 2-3 °C (Fig. 6a). The greenhouse effects contribute to the subtropical
231 warming via increasing surface specific humidity (water vapor; Fig. 6b) and downwelling
232 long-wave radiation (Fig. 6d). The seasonal dependence of specific humidity and long-
233 wave radiatiative flux are also evident and responsible for the enhanced warming during
234 summer (Fig. 6a). Positive sea level pressure deltas at midlatitudes along with weak or
235 negative sea level pressure deltas in subtropics reduce the surface westerly winds (Fig. 6e).
236 The decreased subtropical precipitation (Fig. 6f) and fresh water flux through rivers (river
237 runoff; Fig. 6g) along with the general increase of precipitation and river runoff at mid-to-
238 high latitudes are consistent with the projected expansion of tropical-subtropical dry zone
239 (Lu et al. 2007; Feng and Fu 2013).

240 Seasonal differences in the deltas, defined as half of the difference between the
241 maximum and minimum monthly values, are shown in Fig. 7 for surface air temperature,
242 surface specific humidity and sea level pressure. The observed interannual variations of

243 annual means during 1976-2005 are also shown in Fig 7 for comparison. The seasonal
 244 cycle amplitudes of the deltas are comparable to or larger than the interannual variations
 245 along the continental margins of the NWA, underlying the importance of using seasonally
 246 varying forcing.

247 *d. Downscaling simulations*

248 We performed a 48-year CTRL (yrs. 1958–2005) and RCP85 (equivalent to yrs.
 249 2052-2099) NWA ROMS simulations, and used the last 30 years of each for analyses,
 250 allowing for an 18-year spin-up period. We first assessed the downscaled responses,
 251 obtained from the difference between the RCP85 and CTRL, over the whole NWA domain,
 252 and then present a more detailed analyses of the projections in the Gulf of Maine.

253

254 **3. Downscaled responses over the NWA domain**

255 The downscaled RCP85 responses of SST and surface currents are shown with
 256 those of the GFDL ESM2M in Fig. 8. For the ease of comparison, the GFDL-ESM2M
 257 responses were bilinearly interpolated to the ROMS grid. One consequence of using a high-
 258 resolution ocean model is the redistribution of heat, salt, and momentum. In the wind-
 259 driven ocean circulation where vorticity input (wind stress) balances vorticity dissipation
 260 (lateral diffusion assuming Munk boundary layer; Munk 1950), the thickness of western
 261 boundary layer ε_M is given as $\pi(A_h/\beta)^{1/3}$, where A_h is the horizontal eddy viscosity and
 262 $\beta (= \partial_y f)$ is the variation of Coriolis parameter (f) with latitude. Since ROMS uses 16

263 times smaller eddy viscosity ($25 \text{ m}^2 \text{ s}^{-1}$) than that of the GFDL-ESM2M ocean model (400
 264 $\text{m}^2 \text{ s}^{-1}$), the western boundary layer thickness reduces to $\sim 40 \text{ km}$ from $\sim 100 \text{ km}$. Therefore,
 265 the Gulf Stream is confined to a narrow western boundary layer as shown in Fig. 8. As a
 266 consequence, SST changes become more pronounced around the U.S. east coast in our
 267 downscaled runs compared to the coarse GFDL-ESM2M. Moreover, the maximum speed
 268 of Gulf Stream is further reduced in the downscaled runs.

269 The position shift of Gulf Stream under the RCP 8.5 scenario has been assessed in
 270 the recent study of Saba et al. (2016), who found that a weakened AMOC in the future
 271 leads to a northward shift of the Gulf Stream's separation from the coast. To determine the
 272 position change of Gulf Stream in our downscaled runs, we compare the magnitude of
 273 horizontal gradient of sea surface height (SSH), $\sqrt{(\partial \bar{\eta} / \partial x)^2 + (\partial \bar{\eta} / \partial y)^2}$, in the RCP85
 274 and CTRL in Fig. 9. Many previous studies used the SSH gradient to diagnose the position
 275 of Gulf Stream (e.g. Andres 2016), since the Gulf Stream is better represented as the ocean
 276 transport (in unit of Sv) rather than the Ekman dominated surface current. The ocean is
 277 approximately in geostrophic balance at low frequencies, and the SSH gradient is related
 278 to the geostrophic velocity as $f\mathbf{k} \times \mathbf{u}_g = -g\nabla\eta$ (where g is the acceleration due to gravity
 279 and \mathbf{u}_g is the geostrophic velocity). Thus, the SSH gradient represents the changes in ocean
 280 transport.

281 In contrast to Saba et al. (2016), our downscaled simulations suggest that the Gulf
 282 Stream separation shifts southward under the RCP 8.5 scenario. Other studies also
 283 highlight the lack of consensus on the direction of this shift in response to a change in

284 AMOC; some modeling studies found a northward shift of the Gulf Stream separation in
285 response to a reduction in AMOC, (e.g. Zhang, 2008; Yeager 2015; Saba et al. 2016), while
286 others (e.g. De Coëtlogon et al. 2006; Kwon and Frankignoul 2014) found a southward
287 shift, as in our downscaling simulations.

288 One may wonder if there is a shift in the mean position of zero wind stress curl, so
289 that the southward shift of Gulf Stream is a direct response to the southward shift in zero
290 wind stress curl. In this regard, we compared the long-term mean wind stress curl in CTRL
291 (yrs. 1958-2005) and delta added RCP85 (yrs. 2052-2099) forcings (see Fig. S2 of
292 Supplementary Information). It shows that there is no apparent shift in mean wind stress
293 curl in our simulations. Thus, the southward shift of Gulf Stream cannot be explained by
294 the shift of wind stress curl. Instead, the southward shift of Gulf Stream may be
295 dynamically related to the reduced AMOC via the joint effect of baroclinicity and relief
296 (JEBAR; Mertz and Wright 1992) (see Appendix).

297 The warming of bottom temperatures around the U.S. East Coast is enhanced in the
298 downscaled run compared to the coarse resolution GFDL-ESM2M (Fig. 10). The enhanced
299 warming is pronounced along the continental shelf and shelf break along the Gulf of
300 Mexico and the U.S. East Coast, indicating about a 4°C warming, 1-2°C more than that
301 projected in the coarse resolution GFDL-ESM2M. Enhanced warming of about 1°C over
302 the Gulf of Maine and the Gulf of Saint Lawrence is also evident.

303 In addition to inducing long-term hydrographic changes under the RCP 8.5
304 scenario, the increased radiative forcings also impact the occurrence of ocean eddies. The
305 SSH variance ($\overline{\eta'}^{1/2}$), a measure of eddy activity, is shown in Fig. 11 for the CTRL and the

306 RCP85 simulations during DJF and JJA. Here we decomposed the 5-day mean (pentad)
307 SSH data as the sum of low-pass filtered component and anomaly to this low-passed
308 component as $\eta = \bar{\eta} + \eta'$. The 24-pentad (equivalent to 120-day) running mean, based
309 upon the typical eddy characteristic period over the model domain [50 – 100 days in the
310 Caribbean (Jouanno et al. 2008) and about 90 days for the long-lived eddies in Gulf Stream
311 (Kang and Curchister 2013)] forms the low pass filter.

312 The CTRL simulation captures the observed seasonal cycle of eddy occurrence in
313 the North Atlantic as well as in the Gulf of Mexico (Fig. 11b). Over the Gulf Stream region,
314 eddy activity dominates during summer, though the spatial pattern of eddy activity is
315 similar in summer and winter (e.g. Zhai et al. 2008). As in observations (e.g. Chang and
316 Oey 2012), the Loop Current appears to shed more eddies during summer than in winter in
317 the Gulf of Mexico.

318 The changes of eddies in response to increasing radiative forcing are also larger
319 during summertime, though the main response of the Gulf Stream and Loop Current eddies
320 are very different. While eddy activity along the Gulf Stream indicates a southward shift
321 under the RCP 8.5 scenario consistent with the shift in Gulf Stream separation, Loop
322 Current eddies in the Gulf of Mexico show an increased occurrence under the RCP 8.5
323 scenario.

324 The downscaled results are consistent with the previous studies of Liu et al. (2012;
325 2015) over the Gulf of Mexico: weakening of the Loop Current (Fig. 8) and an intense
326 warming of about 4°C in the continental shelf and shelf break especially during summer
327 (Fig. 10). However, increased eddy activity under the RCP 8.5 scenario (Fig. 11) is

328 inconsistent with Liu et al. (2012, 2015). As noted in Alexander et al. (2019), the
329 experimental design of Liu et al. (2012, 2015) is very different from this study. They used
330 a multi-GCM mean to drive a regional ocean model, and thus retained only the linear
331 component of the climate change forcing. Such difference in experimental design (i.e.
332 climate change forcing) makes it difficult to compare the results side by side. The detailed
333 analysis of Loop Current eddies under the RCP 8.5 scenario remains to be assessed in
334 future studies.

335

336 **4. Coastal environment projections: Gulf of Maine**

337 Here we examine the climatic changes within the Gulf of Maine in greater detail,
338 given the strong warming that has already occurred there and is projected to continue into
339 the future (e.g. Saba et al. 2016; see our Figs. 8 and 10). An accurate representation of the
340 present-day coastal circulation is likely to be critical to obtain the three dimensional
341 structures of changes in the future. As shown in Fig. 1 and S1 (see also the schematics in
342 Fig. 2), our downscaled present-day simulation captures the essence of the Gulf of Maine
343 circulation, including the topographically trapped Gulf of Maine Coastal Plume (GMCP;
344 Keafer et al. 2005) and Maine Coastal Current (MCC; Anderson et al. 2014). It is also clear
345 that the summertime cyclonic MCC forms in combination with Atlantic water that enters
346 the Gulf through the Northeast Channel and exits through the Great South and Northeast
347 channels. The summertime cyclonic MCC is further strengthened in response to RCP8.5
348 forcings (Fig. 12). The warming is amplified along the sill depth of the Northeast Channel,
349 suggesting that a substantial fraction of the warming can be traced to the open ocean.

350 The open ocean influence on the Gulf of Maine is examined further using a cross
351 section at 42°N latitude (Fig. 13), the same cross section as used in Saba et al. (2016). The
352 zonal and vertical velocity changes are shown as vectors, the anomalous northward
353 meridional velocities are dotted, the temperature changes are color shaded, and the salinity
354 differences are contoured. Figure 13 clearly shows the enhanced intrusion of warm and
355 saline open ocean waters into the Gulf through the channel, resulting in warm saline waters
356 at depth in the Gulf. The strengthening of the present-day thermohaline front is also
357 noticeable and may be responsible for the enhanced intrusion of slope waters. These results
358 are qualitatively consistent with the study of Saba et al. (2016), though the magnitudes of
359 changes are much smaller than their estimates.

360 It is also noteworthy that the sources of those warm and salty slope waters may
361 differ between this study and Saba et al. (2016). Observations indicate that the Gulf of
362 Maine waters at depth are composed of a mixture of surface and deep waters flowing into
363 the Gulf: they are Scotian Shelf Water from the Nova Scotian shelf that enters the Gulf at
364 the surface and slope waters that enter at depth through the Northeast Channel (e.g.
365 Townsend et al. 2014). There are two distinct types of slope waters: one is Labrador Slope
366 Water and the other is Atlantic Temperate Slope Water (e.g. Bigelow 1927; Ramp et al.
367 1985; Smith et al. 2001; Townsend et al. 2014; Townsend et al. 2015).

368 To highlight the source water masses that impact the Gulf of Maine in the CTRL
369 and RCP85 simulations, we estimated the backward trajectory of particles by using
370 TRACMASS (Döös 1995; Döös et al. 2017; <http://tracmass.org>) on the output of the
371 currents from both ROMS simulations. We initialized 1,521 particles at 5-day intervals

372 from June 2nd to August 31st (a total of 28,899 particles) over the region (41.63-44.61°N;
373 69.90-65.96°W; thick black box in Fig. 14) between the depths of 145 and 327 m. These
374 particles were tracked backward by using the mean annual cycle of three-dimensional
375 velocities at a daily time resolution. While the zonal and meridional velocities were
376 obtained from the CTRL and RCP85 runs, the mean annual cycle of vertical velocity was
377 estimated using the continuity equation. Then, the TRACMASS model was integrated
378 backward for 1,000 days starting from August 31st.

379 The water masses that contribute to Gulf of Maine bottom waters in the current
380 climate settings are illustrated in Fig. 14 by randomly choosing 20 particle trajectories. It
381 largely conforms to previous studies on the composition of Gulf of Maine bottom waters,
382 which consist of a mixture of Atlantic Temperate Slope Waters (Gulf Stream), Labrador
383 Subarctic Slope Waters, and Scotian Shelf Waters. There is also substantial recirculation
384 of Gulf Stream waters before they enter the Gulf of Maine.

385 The maps of instantaneous particle density in CTRL and RCP85 runs at 200, 500,
386 and 1,000 days before the initial time (August 31st) are shown in Fig. 15 (see movie clip,
387 Fig. S3 of Supplementary Information, for time varying maps of particle density). We
388 estimated the particle density by counting the number of particles over the whole water
389 column within 1° x 1° grid boxes. At the first 200-day backward tracking, the Gulf of Maine
390 bottom waters are mostly influenced by the Scotian Shelf Waters. Further back in time
391 (500 and 1,000 days before the initial time), the Labrador Subarctic Slope Waters and, to
392 a lesser extent, Atlantic Temperate Slope Waters impact the composition of Gulf of Maine
393 bottom waters.

394 The percentage change of particle densities over time (instantaneous number of
395 particles divided by initial number of particles) over the Gulf of Maine, subtropical N.
396 Atlantic ($\leq 36^{\circ}\text{N}$), and subpolar N. Atlantic ($> 36^{\circ}\text{N}$) are shown in Fig. 16. During the
397 1,000-day backward integration of TRACMASS, contributions from the subtropical N.
398 Atlantic (i.e. Atlantic Temperate Slope Waters) are negligible compared to the subpolar N.
399 Atlantic (i.e. Labrador Subarctic Slope Waters). There is substantial recirculation of Gulf
400 Stream Waters before entering into the Gulf of Maine (see Fig. 14), and thus the Atlantic
401 Temperate Slope Waters may lose their characteristics by intense mixing before impacting
402 the Gulf of Maine bottom waters.

403 Figures 15 and 16 indicate that the source waters for the Gulf Maine are very similar
404 in the CTRL and RCP8.5, including the absence of Gulf Stream waters in the latter. Then
405 why does the Gulf of Maine warm so intensively in the future? The answer may lie in
406 where the temperatures change the most over the N. Atlantic, rather than on where the
407 water originated from. In this regard, the intense warming southeast of Newfoundland in
408 response to increased radiative forcing appears in most coupled climate model simulations
409 (e.g. Alexander et al. 2019), including the GFDL-ESM2M. Indeed, the change in
410 temperature between 2070-2099 and 1976-2005 exceeds 5°C at the surface and 8°C at 200
411 m depth in the vicinity of 46°N , 45°W in GFDL-ESM2M RCP 8.5 simulation (Alexander
412 et al. 2019). The backward particle trajectory results suggest that this very warm water is
413 transported to the Gulf of Maine, and thus the Gulf of Maine warming is predominately
414 forced by changes in the source water properties rather than changes in source water
415 contributions.

416

417 **5. Summary and concluding remarks**

418 In this study, we downscaled the GFDL-ESM2M projected ocean climate changes
419 along the U.S. East and Gulf coasts using ROMS, an eddy-resolving regional ocean model.
420 The large-scale climate change forcings were obtained from the mean difference (i.e.
421 deltas) between the period yrs. 2070-2099 and yrs. 1976-2005. We extended previous
422 versions of this method (e.g. Auad et al. 2006; Liu et al. 2012; van Hooidonk et al. 2015)
423 by including a seasonal cycle of the deltas to address the strong seasonal dependence of
424 climate change (e.g., Partanen et al. 2017). While the delta method removes the mean
425 (present-day) bias and enhances the signal-to-noise ratio of the response, it neglects
426 changes in interannual climate variability. Therefore, our approach can be viewed as a
427 sensitivity test of the response of the coastal ocean to future changes in radiation.

428 The downscaled climate projection indicates enhanced warming of ocean bottom
429 temperatures relative to the global climate model around the U.S. East and Gulf coasts,
430 particularly along the continental shelf and shelf break. Enhanced warming also occurs in
431 the Gulf of Maine and Gulf of Saint Lawrence. We attribute the enhanced warming to the
432 improved simulations of coastal ocean hydrography in ROMS. The ROMS control
433 simulation resolved the essence of observed coastal ocean circulation. For example, ROMS
434 captures the topographically trapped GMCP and MCC in the Gulf of Maine and intrusion
435 of open ocean waters through the Northeast Channel. In response to increasing radiative
436 forcing, the intrusion of slope waters is increased and summertime cyclonic MCC is further

437 strengthened. This leads to enhanced warming in the Gulf of Maine preferentially at depth
438 following the sill depth of Northeast Channel, consistent with Saba et al. (2016).

439 However, in contrast to Saba et al. (2016), we find that the role of Atlantic
440 Temperate Slope Waters (Gulf Stream Waters) on projected warming at depth in the Gulf
441 of Maine is relatively minor compared to the contribution of Labrador Subarctic Slope
442 Waters. Backward trajectories of particles indicate that Gulf of Maine waters can originate
443 primarily from the subpolar N. Atlantic rather than the subtropics. Given the dramatic
444 warming off the coast of Newfoundland and Labrador in climate projections, our results
445 suggest this advective pathway as a key driver for the projected Gulf of Maine warming.
446 Thus, monitoring and modeling of the subpolar N. Atlantic are crucial to improve our
447 understanding of changes in the Gulf of Maine.

448 In closing, some previous studies (e.g. Brooks 1987) suggested the important role
449 of eddies in hydrographic changes over the Gulf of Maine. For example, occasional
450 propagations of Gulf Stream warm core rings into the regions impact Gulf of Maine
451 temperatures at depth by modifying the characteristics of slope waters. Our downscaled
452 projection shows substantial changes in eddies in response to RCP 8.5 radiative forcings.
453 However, the detailed dynamical linkage between the Gulf Stream eddies and the
454 hydrographic changes over the Gulf of Maine, and the relative importance of the eddy
455 impacts on the mean circulation changes remains to be assessed in future studies.

456

457 *Acknowledgment.* This work was supported by NOAA/CPO COCA program, grant #NA-

458 15OAR4310133. We thank Drs. Charles Stock and Enrique Curchitser for discussion on
 459 the results. We also thank Dr. Michael Jacox for his insightful comments on the manuscript.

460

461 APPENDIX A

462 **Path of Gulf Stream .vs. Strength of AMOC**

463 Observational (e.g. Peña-Molino and Joyce 2008) and modeling studies (e.g. De
 464 Coëtlogon et al. 2006; Zhang 2008; Kwon and Frankignoul 2014; Yeager 2015) indicate
 465 that the path of Gulf Stream and the strength of AMOC are dynamically linked, although
 466 the direction of relationship is still in debate. For example, in response to reduced AMOC,
 467 some modeling studies (e.g. Zhang 2008; Yeager 2015) suggest a northward shift of Gulf
 468 Stream, while others (e.g. De Coëtlogon et al. 2006; Kwon and Frankignoul 2014) suggest
 469 the opposite. Observations appear to support the former (e.g. Peña-Molino and Joyce 2008;
 470 Wu et al. 2012), though the limited length of data obscures any statistical significance [see
 471 Fig. 8 of Saba et al. (2016)].

472 Zhang and Vallis (2007) provide a simple dynamical explanation of how the path
 473 of Gulf Stream can be tied to the AMOC strength by using a vertically integrated vorticity
 474 equation in the presence of ocean topography. For example, in the presence of a linear
 475 zonal slope of height z_b at its western edge sloping downward to zero at a point in the basin
 476 x_b ,

$$477 z_b(x) = \begin{cases} z(x_b - x) & 0 \leq x \leq x_b \\ 0 & \text{otherwise} \end{cases}, \text{ where } z > 0, \quad (\text{A1})$$

478 the steady barotropic vorticity equation over the inviscid ocean interior can be written as
 479 $\beta \partial_x \psi_B = f_0 (W_E - W_B) / H$. Where H is the undisturbed flat ocean depth, the Coriolis
 480 parameter, f , varies linearly with latitude using the β -plane, W_E denotes the surface
 481 Ekman pumping, and $W_B = J(\psi_B, z_b) = \partial_x \psi_B \partial_y z_b - \partial_x z_b \partial_y \psi_B$ denotes barotropic vortex
 482 stretching/compression due to the interaction between ocean circulation and the underlying
 483 topography. By integrating the equation from the eastern boundary ($x = L$), the total
 484 interior transport ψ_B can be obtained as the sum of (i) the Sverdrup transport Ψ and (ii)
 485 the transport induced by bottom vortex stretching ψ_{W_B} :

$$486 \quad \psi_B = \Psi + \psi_{W_B} = \underbrace{-\frac{f_0}{\beta H} \int_x^L W_E dx}_{(i)} + \underbrace{\frac{f_0}{\beta H} \int_x^L W_B dx}_{(ii)}. \quad (\text{A2})$$

487 At the gyre boundary ($\psi_B = 0$) with any observation-like Ekman pumping, $W_B < 0$, and
 488 thus $\psi_{W_B} < 0$. Therefore the western boundary current tends to separate over the regions
 489 where $\Psi > 0$ (i.e. south of zero wind stress curl line) due to the bottom vortex stretching to
 490 satisfy $\psi_B = 0$.

491 Zhang and Vallis (2007) further investigated how variations in AMOC strength
 492 could influence the Gulf Stream via changes in bottom vortex stretching. The method they
 493 used was to diagnose the bottom vortex stretching term from a primitive equation ocean
 494 model, and then prescribe it as a bottom boundary forcing in a barotropic Quasi-
 495 Geostrophic (QG) ocean model. Their results suggest that a reduced AMOC induces less
 496 bottom vortex stretching resulting in a northward shift of western boundary current;

497 however, by design, the JEBAR (Mertz and Wright 1992) was not interactive in their
 498 model.

499 To incorporate the effects of JEBAR interactively, we used a two-layer eddy-
 500 resolving QG model with bottom topography (z_b ; see A1), the ocean component of QG
 501 Coupled Model (Q-GCM; Hogg et al. 2003). The vertical buoyancy fluxes between the
 502 two layers represented as interfacial mass flux (w_s) over an idealized square shape ocean
 503 in midlatitude. The domain dimensions are $L \times L$ and the mean layer thicknesses of the
 504 upper and lower layers are H_1 and H_2 respectively. The equation for the evolution of QG
 505 Potential Vorticity (QGPV) anomaly (q) and the associated elliptic equation for velocity
 506 streamfunction (ψ) in each layer are

$$\begin{aligned} \partial_t q_1 + J(\psi_1, q_1) &= \frac{f_0}{H_1} (w_e - w_s) + A_H \nabla^6 \psi_1 \\ \partial_t q_2 + J(\psi_2, q_2) &= \frac{f_0}{H_2} w_s + A_H \nabla^6 \psi_2 - \sigma \nabla^2 \psi_2 \\ q_1 &= \nabla^2 \psi_1 + \beta y + \frac{f_0^2}{g' H_1} (\psi_2 - \psi_1) \\ q_2 &= \nabla^2 \psi_2 + \beta y + \frac{f_0^2}{g' H_2} (\psi_1 - \psi_2) + \frac{f_0}{H_2} z_b \end{aligned}, \quad (A3)$$

507 where w_e is the surface Ekman pumping, A_H and σ are the biharmonic diffusion and linear
 508 bottom friction coefficients. Here, we used the analytic forms of w_e (e.g. Karabasov et al.
 509 2009) and w_s (e.g. Wu et al. 1999):

$$\begin{aligned}
511 \quad w_e(x,y) = & \begin{cases} -W_E \sin\left(\pi \frac{y}{y_e}\right) & 0 \leq y < y_e \\ W_E \sin\left(\pi \frac{y-y_e}{L-y_e}\right) & y_e \leq y \leq L \end{cases} \quad \frac{y_e}{L} = 0.5 + 0.2\left(\frac{x}{L} - 0.5\right) \\
w_s(y) = & \theta \left[1 - e^{\frac{\mu}{L}(y-y_s)} \right] \sin\left(\pi \frac{y}{L}\right) \quad \frac{y_s}{L} = 0.8
\end{aligned} \quad . \quad (\text{A4})$$

512 Where W_E is the amplitude of Ekman pumping scaled to yield an observed interior
513 Sverdrup transport of 30 Sv [i.e. $\Psi = f_0 W_E L / (\beta H)$] in the North Atlantic. The parameter
514 y_e controls the asymmetry of w_e relative to the mid-axis of the basin ($y = 0.5L$), and is
515 designed to avoid artificial gyre symmetry. The parameter y_s separates a narrow intense
516 sinking at highlatitudes from a broad upwelling elsewhere as conceptualized by Stommel
517 et al. (1958). With predetermined y_s and the total sinking mass flux Q_0 (the same as total
518 upwelling flux to satisfy mass conservation; $Q_0 = \varepsilon \Psi L \int_{y_s}^L |w_s| dy = \varepsilon \Psi L \int_0^{y_s} w_s dy$, where
519 $\varepsilon = \beta L / f_0$), unique μ and θ are determined. The meridional distributions of w_e and w_s
520 are shown in Fig. A1, and the standard values of parameters used are summarized in Table
521 A1. Free-slip conditions are applied to all lateral boundaries. All numerical experiments
522 were integrated for 200 years, and the last 100 years were used to estimate time-averaged
523 flow patterns.

524 A set of QG model experiments was performed by reducing the magnitude of total
525 sinking mass flux Q from $Q_0 (= 7.5 \text{ Sv})$ to 0 Sv, while keeping its meridional profile. The
526 resulting barotropic flow patterns over the slope are shown in Fig. A2a. It clearly indicates
527 that the path of western boundary current shifts southward as AMOC weakens, consistent

528 with our downscaled results and the previous modeling studies (De Coëtlogon et al. 2006;
529 Kwon and Frankignoul 2014).

530 Could the result shown in Fig. A2a be an artifact of the prescribed profiles of w_e
531 and w_s ? Mathematically, w_s for the upper layer acts like w_e [see the term $\sim (w_e - w_s)$ in the
532 first equation of (A3)], and the net impact of decreased w_s (i.e. weakened AMOC) is the
533 same as shifting zero wind stress curl line southward. Thus, the conceptual model for deep-
534 ocean circulation based upon Stommel et al. (1958) connotes the relationship of increased
535 bottom vortex stretching due to weakened AMOC by design. To address this issue, we
536 performed another set of QG model experiments. In this case, the narrow intense sinking
537 at highlatitudes from y_s to L is balanced by narrow intense upwelling of equal area at the
538 regions of southern boundary spanning the equal area from 0 to y_s^* ($= 0.2 L$) to maintain
539 the position of zero wind stress curl line during the experiments.

540 The results shown in Fig. A2b are qualitatively similar to those in Fig. A2a,
541 although the southward shift of western boundary current is not as dramatic. However, note
542 that the typical western boundary current shift in coupled climate models, if present, is only
543 few degrees in latitude even in the case of CO₂ doubling. That is only about 5 % (1-2° in
544 latitude) of the meridional extent of the subtropical gyre (about 30° in latitude) (Saba et al.
545 2016). Moreover, Fig. A2b shows the weakening of subtropical gyre as AMOC decreases.
546 That is consistent with our downscaled simulations. Although simulating the detailed
547 structure of the deep-ocean circulation is clearly beyond the scope of this study, the general
548 findings appear robust, i.e. the path of western boundary current shifts southward as
549 AMOC weakens.

550 **REFERENCES**

- 551 Alexander, M., S.-I. Shin, J. D. Scott, E. Curchitser, and C. Stock, 2019: The response of
552 the northwest Atlantic Ocean to climate change. *J. Climate*, submitted. (available
553 at <https://www.esrl.noaa.gov/psd/people/michael.alexander/publications.html>).
- 554 Anderson, D. L., and Coauthors, 2004: The new GFDL global atmosphere and land model
555 AM2-LM2: Evaluation with prescribed SST simulations. *J. Climate*, **17**, 4641–
556 4673.
- 557 Anderson, D. M., and Coauthors, 2014: Understanding interannual, decadal level
558 variability in paralytic shellfish poisoning toxicity in the Gulf of Maine: The HAB
559 index. *Deep-Sea Res. II*, **103**, 264–276.
- 560 Andres, M., 2016: On the recent destabilization of the Gulf Stream path downstream of
561 Cape Hatteras. *Geophys. Res. Lett.*, **43**, doi:10.1002/2016GL069966.
- 562 Auad, G, A. Miller, and E. Di Lorenzo, 2006: Long-term forecast of oceanic conditions off
563 California and their biological implications. *J. Geophys. Res.*, **111**, C09008,
564 doi:10.1029/2005JC003219.
- 565 Bigelow, H. B., 1927: Physical oceanography of the Gulf of Maine. *Bull. U.S. Bur. Fish.*,
566 **40**, 511–1027.
- 567 Bonjean, F., and G. S. E. Lagerloef, 2002: Diagnostic model and analysis of the surface
568 currents in the tropical Pacific Ocean. *J. Phys. Oceanogr.*, **32**, 2938–2954.

- 569 Brooks, D. A., 1987: The influence of warm-core rings on the slope water entering the Gulf
570 of Maine. *J. Geophys. Res.*, **92**, 8183–8196.
- 571 Buckley, M. and J. Marshall, 2016: Observations, inferences, and mechanisms of the
572 Atlantic Meridional Overturning Circulation: A review. *Rev. Geophys.*, **54**, 5–63.
- 573 Caesar, L., S. Rahmstorf, A. Robinson, G. Feulner, and V. Saba, 2018: Observed
574 fingerprint of a weakening Atlantic Ocean overturning circulation. *Nature*, **256**,
575 191–196.
- 576 Carton, J. A., and B. S. Giese, 2008: A reanalysis of ocean climate using Simple Ocean
577 Data Assimilation (SODA). *Mon. Wea. Rev.*, **136**, 2999–3017.
- 578 Chang, Y.-L., and L.-Y. Oey, 2012: Why does the Loop Current tend to shed more eddies
579 in summer and winter? *Geophys. Res. Lett.*, **39**, L05605,
580 doi:10.1029/2011GL050773.
- 581 Cheng, W., J. C. H. Chiang, and D. Zhang, 2013: Atlantic Meridional Overturning
582 Circulation (AMOC) in CMIP5 models: RCP and historical simulations. *J. Climate*,
583 **26**, 7187–7197.
- 584 Curchitser, E. N., D. B. Haidvogel, A. J. Hermann, E. Dobbins, T. M. Powell, and A.
585 Kaplan, 2005: Multi-scale modeling of the North Pacific Ocean: Assessment of
586 simulated basin-scale Variability (1996–2003). *J. Geophys. Res.*, **110**, C11021,
587 doi:10.1029/2005JC002902.

- 588 Dai, A., T. Qian, K. E. Trenberth, and J. D. Milliman, 2009: Changes in continental
589 freshwater discharge from 1948–2004. *J. Climate*, **22**, 2773–2792.
- 590 De Coëtlogon, G., C. Frankignoul, M. Bentsen, C. Delon, H. Haak, S. Masina, and A.
591 Pardaens, 2006: Gulf Stream variability in five ocean general circulation models.
592 *J. Phys. Oceanogr.*, **36**, 2119–2135.
- 593 Döös, K., 1995: Inter-ocean exchange of water masses. *J. Geophys. Res.*, **100**, 13499–
594 13514.
- 595 Döös, K., B. Jönsson, and J. Kjellsson, 2017: Evaluation of oceanic and atmospheric
596 trajectory schemes in the TRACMASS trajectory model v6.0. *Geosci. Model Dev.*,
597 **10**, 1733–1749.
- 598 Dunne, J. P., and Coauthors, 2012: GFDL’s ESM2 Global Coupled Climate–Carbon Earth
599 System Models. Part I: Physical Formulation and Baseline Simulation
600 Characteristics. *J. Climate*, **25**, 6646–6665.
- 601 Feng, S., and Q. Fu, 2013: Expansion of global drylands under a warming climate. *Atmos.*
602 *Chem. Phys.*, **13**, 10081–10094.
- 603 Griffies, S. M., and Coauthors, 2005: Formulation of an ocean model for global climate
604 simulations. *Ocean Sci.*, **1**, 45–79.
- 605 Griffies, S. M., and Coauthors, 2015: Impacts on ocean heat from transient mesoscale
606 eddies in a hierarchy of climate models. *J. Climate*, **28**, 952–977.

- 607 He, J., and B. J. Soden, 2016: The impact of SST biases on projections of anthropogenic
608 climate change: A greater role for atmosphere-only models? *Geophys. Res. Lett.*,
609 **43**, 7745-7750.
- 610 Hoegh-Guldberg, O., and J. F. Bruno, 2010: The impact of climate change on the world's
611 marine ecosystems. *Science*, **328**, 1523-1528.
- 612 Hogg, A. M., J. R. Blundell, W. K. Dewar, and P. D. Killworth, 2003: Formulation and
613 users' guide for Q-GCM (version 1.0). Southampton Oceanography Centre,
614 Internal Document No. 88, Most recent version available from [http://www.q-](http://www.q-gcm.org)
615 [gcm.org](http://www.q-gcm.org).
- 616 IPCC, 2013: Climate Change 2013: The Physical Science Basis. Contribution of Working
617 Group I to the Fifth Assessment Report of the Intergovernmental Panel on Climate
618 Change [Stocker, T. F., D. Qin, G.-K. Plattner, M. Tignor, S. K. Allen, J. Boschung,
619 A. Nauels, Y. Xia, V. Bex and P. M. Midgley (eds.)]. Cambridge University Press,
620 Cambridge, United Kingdom and New York, NY, USA, 1535 pp.
- 621 Kang, D., and E. N. Curchister, 2013: Gulf Stream eddy characteristics in a high-resolution
622 ocean model. *J. Geophys. Res.*, **118**, 4474-4487.
- 623 Kang, D., and E. N. Curchitser, 2015: Energetics of eddy-mean flow interactions in the
624 Gulf Stream region. *J. Phys. Oceanogr.*, **45**, 1103-1120.
- 625 Karabasov, S. A., P. S. Berloff, and V. M. Goloviznin, 2009: CABARET in the ocean
626 gyres. *Ocean Model.*, **30**, 155-168.

- 627 Keafer, B. A., J. H. Churchill, D. J. McGillicuddy Jr., D. M. Anderson, 2005: Bloom
628 development and transport of toxic *Alexandrium fundyense* populations within a
629 coastal plume in the Gulf of Maine. *Deep-Sea Res. II*, **52**, 2674–2697.
- 630 Kwon, Y.-O., and C. Frankignoul, 2014: Mechanisms of multidecadal Atlantic meridional
631 overturning circulation variability diagnosed in depth versus density space. *J.
632 Climate*, **27**, 9359-9376.
- 633 Jouanno, J., J. Sheinbaum, B. Barnier, J.-M. Molines, L. Debreu, and F. Lemarié, 2008:
634 The mesoscale variability in the Caribbean Sea. Part I: Simulations and
635 characteristics with an embedded model. *Ocean Model.*, **23**, 82–101.
- 636 Large, W. G., and S. G. Yeager, 2009: The global climatology of an interannually varying
637 air-sea flux data set. *Clim. Dyn.*, **33**, 341–364.
- 638 Le Bris, A., and Coauthors, 2017: Climate vulnerability and resilience in the most valuable
639 North American fishery. *PNAS*, **115**, 1831-1836.
- 640 Liu, Y., S.-K. Lee, B. A. Muhling, J. T. Lamkin and D.B. Enfield, 2012: Significant
641 reduction of the Loop Current in the 21st century and its impact on the Gulf of
642 Mexico. *J. Geophys. Res.*, **117**, C05039.
- 643 Liu, Y., S.-K. Lee, D. B. Enfield, B. A. Muhling, J. T. Lamkin, F. Muller-Karger and M.
644 A. Roffer, 2015: Potential impact of climate change on the Intra-Americas Seas:
645 Part-1. A dynamic downscaling of the CMIP5 model projections. *J. Marine Syst.*,
646 **148**, 56-69.

- 647 Lu, J., G. A. Vecchi, and T. Reichler, 2007: Expansion of the Hadley cell under global
648 warming. *Geophys. Res. Lett.*, **34**, L06805, doi:10.1029/2006GL028443.
- 649 Lumpkin, R., and G. C. Johnson, 2013: Global ocean surface velocities from drifters:
650 Mean, variance, El Nino–Southern Oscillation response, and seasonal cycle. *J.
651 Geophys. Res. Oceans*, **118**, 2992–3006.
- 652 Mertz, G., and G. D. Wright, 1992: Interpretation of the JEBAR term. *J. Phys. Oceanogr.*,
653 **22**, 301-305.
- 654 Minobe, S., M. Terada, B. Qiu, and N. Schneider, 2017: Western boundary sea level: A
655 theory, rule of thumb, and application to climate models. *J. Phys. Oceanogr.*, **47**,
656 957-977.
- 657 Munk, W. H., 1950: On the wind-driven ocean circulation. *J. Meteor.*, **7**, 79-93.
- 658 Partanen, A.-I., M. Leduc, and H. D. Matthews, 2017: Seasonal climate change patterns
659 due to cumulative CO₂ emissions. *Environ. Res. Lett.*, **12**, 075002.
- 660 Peña-Molino, B., and T. M. Joyce, 2008: Variability in the slope water and its relation to
661 Gulf Stream path. *Geophys. Res. Lett.*, **35**, L03606, doi:10.1029/2007GL032183.
- 662 Pershing, A. J., and Coauthors, 2015: Slow adaptation in the face of rapid warming leads
663 to collapse of the Gulf of Maine cod fishery. *Science*, **350**, 809-812.
- 664 Ramp, S. R., R. J. Schlitz, and W. R. Wright, 1985: The deep flows through the Northeast
665 Channel, Gulf of Maine. *J. Phys. Oceanogr.*, **15**, 1790–1808.

- 666 Saba, V. S., and Coauthors, 2016: Enhanced warming of the Northwest Atlantic Ocean
667 under climate change. *J. Geophys. Res. Oceans*, **121**, 118–132.
- 668 Shchepetkin, A. F., and J. C. McWilliams, 2005: The Regional Oceanic Modeling System
669 (ROMS): A split-explicit, free-surface, topography-following-coordinate oceanic
670 model. *Ocean Modell.*, **9**, 347–404.
- 671 Small, R. J., and Coauthors, 2014: A new synoptic scale resolving global climate
672 simulation using the Community Earth System Model. *J. Adv. Model. Earth Syst.*,
673 **6**, 1065–1094.
- 674 Smith P. C., W. W. Houghton, R. G. Fairbanks, and D. G. Mountain, 2001: Interannual
675 variability of boundary fluxes and water mass properties in the Gulf of Maine and
676 on Georges Bank: 1993–1997. *Deep-Sea Res. II*, **48**, 37–70.
- 677 Stommel H., A.B. Arons, and A.J. Faller, 1958: Some examples of stationary flow patterns
678 in bounded basins. *Tellus*, **10**, 179–187.
- 679 Taylor, K. E., R. J. Stouffer, and G. A. Meehl, 2012: An overview of CMIP5 and the
680 experiment design. *Bull. Amer. Meteor. Soc.*, **93**, 485–498.
- 681 Townsend, D. W., D. J. McGillicuddy Jr., M. A. Thomas, and N. D. Rebuck, 2014:
682 Nutrients and water masses in the Gulf of Maine–Georges Bank region: Variability
683 and importance to blooms of the toxic dinoflagellate *Alexandrium fundyense*. *Deep-*
684 *Sea Res. II*, **103**, 238–263.

- 685 Townsend, D. W., and Coauthors, 2015: Water masses and nutrient sources to the Gulf of
686 Maine. *J. Mar. Res.*, **73**, 93-122.
- 687 van Hoiddonk, R., J. A. Maynard, Y. Liu, and S.-K. Lee, 2015: Downscaled projections of
688 Caribbean coral bleaching that can inform conservation planning. *Global Change
689 Biol.*, **21**, 3389-3401.
- 690 Wu, L., Z. Liu, and H. E. Hurlburt, 1999: The effect of continental slope on buoyancy-
691 driven circulation. *J. Phys. Oceanogr.*, **29**, 1881-1891.
- 692 Wu, L., W. Cai, L. Zhang, H. Nakamura, A. Timmermann, T. Joyce, M. J. McPhaden, M.
693 Alexander, B. Qiu, M. Visbeck, P. Chang, and B. Giese, 2012: Enhanced warming
694 over the global subtropical western boundary currents. *Nature Climate Change*,
695 DOI: 10.1038/NCLIMATE1353.
- 696 Yeager, S., 2015: Topographic coupling of the Atlantic overturning and gyre circulations.
697 *J. Phys. Oceanogr.*, **45**, 1258-1284.
- 698 Zhai, X., R. J. Greatbatch, and J.-D. Kohlmann, 2008: On the seasonal variability of eddy
699 kinetic energy in the Gulf Stream region. *Geophys. Res. Lett.*, **35**, L24609,
700 doi:10.1029/2008GL036412.
- 701 Zhang, R., and G. K. Vallis, 2007: The role of bottom vortex stretching on the path of the
702 North Atlantic western boundary current and on the northern recirculation gyre. *J.
703 Phys. Oceanogr.*, **37**, 2053-2080.

704 Zhang, R., 2008: Coherent surface-subsurface fingerprint of the Atlantic meridional
705 overturning circulation. *Geophys. Res. Lett.*, **35**, L20705,
706 doi:10.1029/2008GL035463.

707

708

709 **Table 1.** Atmospheric forcing variables used to estimate seasonally varying delta.

ROMS (GFDL- ESM2M)*	Description	Units	Resolution
pair (psl)	Sea Level Pressure	Pa	
qair (huss)	Surface Specific Humidity	kg kg ⁻¹	
tair (tas)	Surface Air Temperature	°C	
uwind (uas)	10 m U-wind Component	m s ⁻¹	
vwind (vas)	10 m V-wind Component	m s ⁻¹	T63
lwrad_down (rlds)	Downwelling LW Radiation	W m ⁻²	(CORE2)
sward (rsds)	Downwelling SW Radiation	W m ⁻²	
rain (pr)	Rainfall Rate	kg (m ⁻² s ⁻¹)	
runoff (friver)	River Runoff	kg (m ⁻² s ⁻¹)	Dai & Trenberth Discharge Grid

710 * Here we followed the nomenclature of ROMS (CMIP5) standard.

711

712

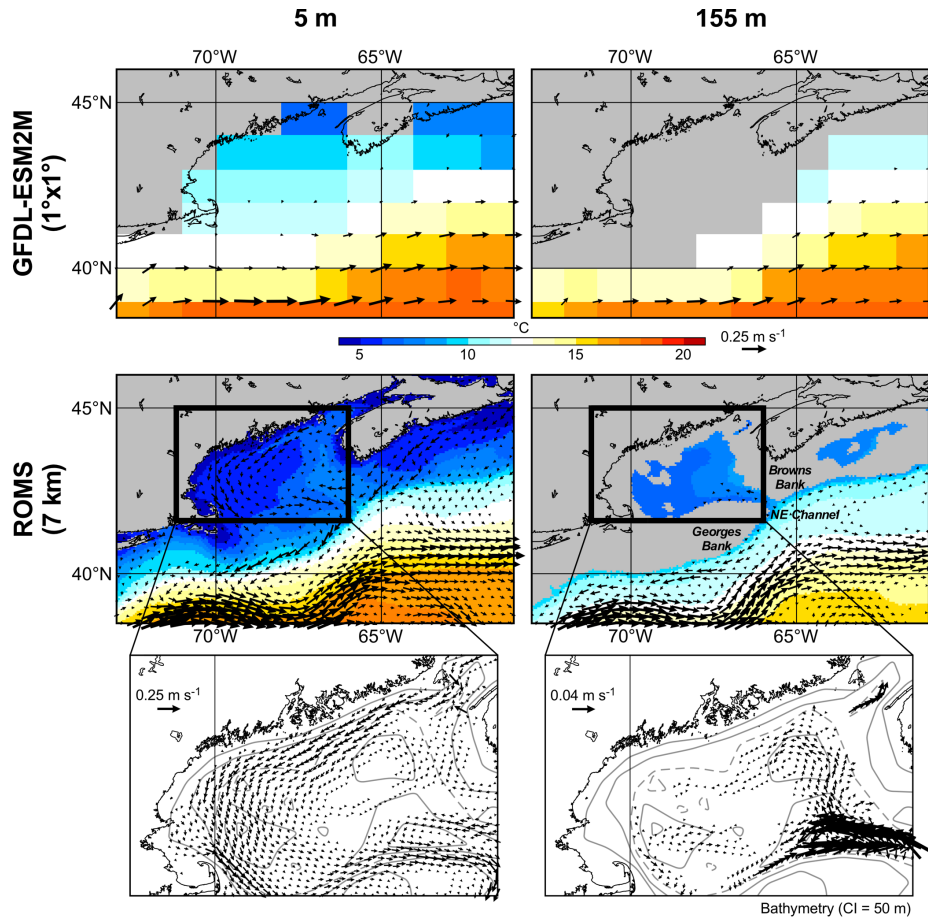
713 **Table A1.** Parameters used in 2-layer eddy resolving QG model.

Basin Domain ($L \times L$)	(4,000 km \times 4,000 km)
Layer Thickness (H_1, H_2)	(1,000 m, 3,000 m)
Total Depth (H)	4,000 m
Maximum Slope Height (Z)	1,000 m
Zonal Extent of Slope (x_b)	1,000 km
Coriolis Parameter ($f = f_0 + \beta y$)	$f_0 = 1 \times 10^{-4}$ s ⁻¹ $\beta = 2 \times 10^{-11}$ m ⁻¹ s ⁻¹
Reduced Gravity	$g' = g \frac{\Delta \rho}{\rho_0} = 0.02$ m s ⁻²
Biharmonic Dissipation Coeff.	$A_H = 2 \times 10^{10}$ m ⁴ s ⁻¹
Bottom Friction Coeff.	$\sigma = 1 \times 10^{-7}$ s ⁻¹
Resolution	10 km
Time Step	30 min
Total Sinking Mass Flux (Q_0)	7.5 Sv

714

715

1



2

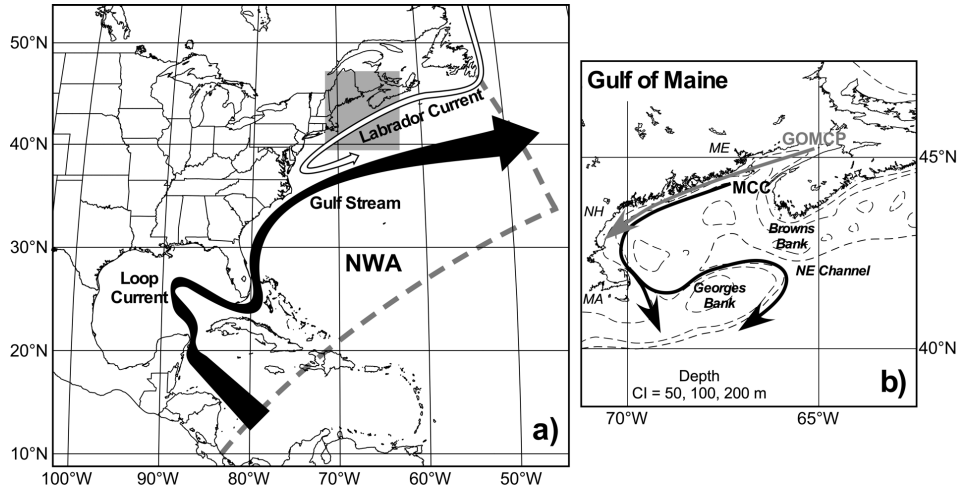
3 **Fig. 1.** (left) Wintertime (DJF) temperature (shading) and currents (arrows) at 5 m
 4 depth over the Gulf of Maine during the yrs. 1976-2005 derived from (top) the
 5 coarse resolution GFDL ESM2M and (bottom) the fine resolution ROMS.
 6 (right) The same as the left but for the patterns at depth (155 m).

7

8

9

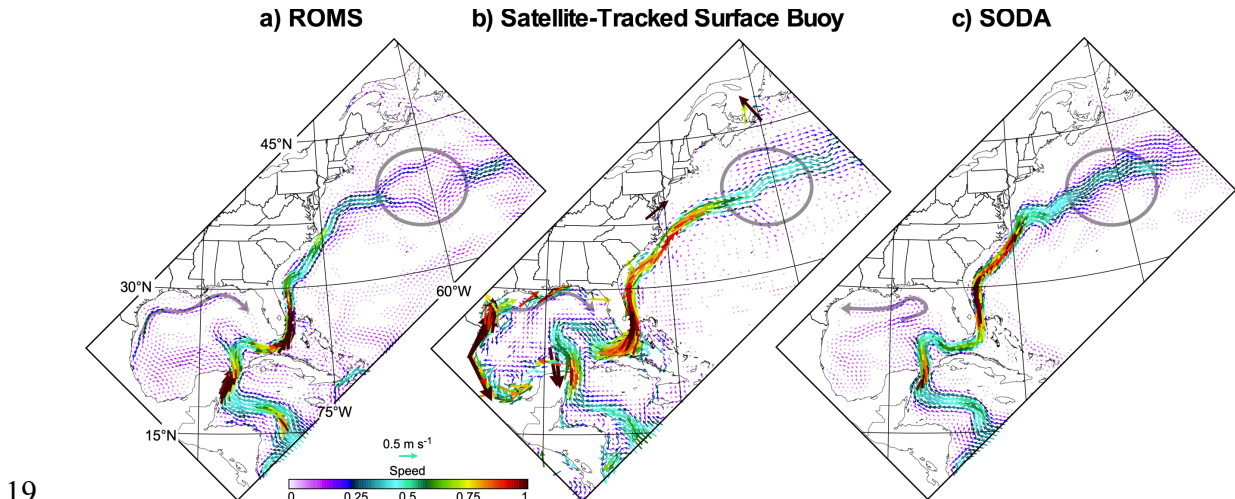
10



11 **Fig. 2.** a) Schematics of major current systems in our downscaling domain covers the
 12 Northwest Atlantic Ocean and Gulf of Mexico (NWA). Thick gray dashed line
 13 indicates the position of open boundaries of NWA. b) Major current systems in
 14 Gulf of Maine (denoted as gray shading in a) shown with solid arrows: black -
 15 Maine Coastal Current (MCC); grey - Gulf of Maine Coastal Plume (GMCP).
 16 Abbreviations used: MA – Massachusetts; NH – New Hampshire; ME – Maine.

17

18



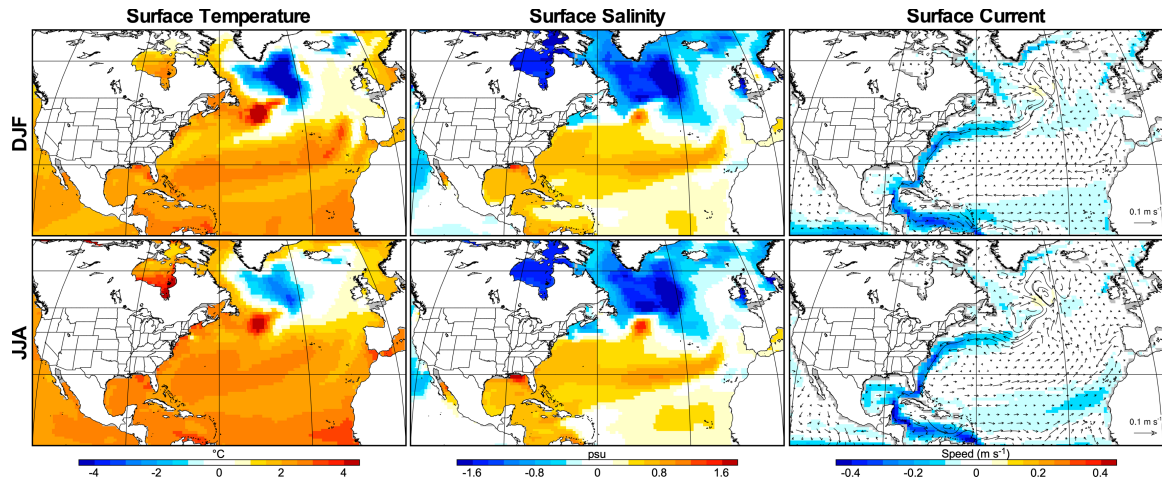
19

20 **Fig. 3.** Maps of annually averaged surface current derived from a) ROMS CTRL
 21 (averaged over during yrs. 1976-2005), b) satellite-tracked surface buoy dataset
 22 (averaged over during January 1979 - March 2015; Lumpkin and Johnson
 23 2013), and c) SODA version 2.1.6 dataset (averaged over during yrs. 1976-
 24 2005). The colors indicate the speed of surface current. The gray circle and gray
 25 line with arrow highlight the exaggerated Gulf Stream split in ROMS and a
 26 clockwise coastal circulation over the Gulf of Mexico, respectively.

27

28

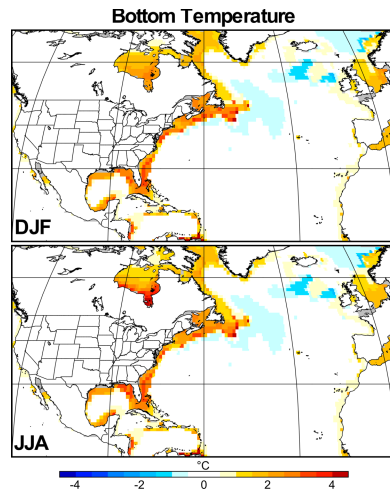
29



30 **Fig. 4.** (top) Maps of DJF GFDL-ESM2M responses of ocean surface (left)
 31 temperature, (middle) salinity, and (right) current to RCP 8.5 radiative forcing
 32 changes, estimated as the mean differences between two time periods
 33 representing future (yrs. 2070-2099) and present-day (yrs. 1976-2007) climate
 34 conditions. (bottom) The same as the top but for the JJA.

35

36

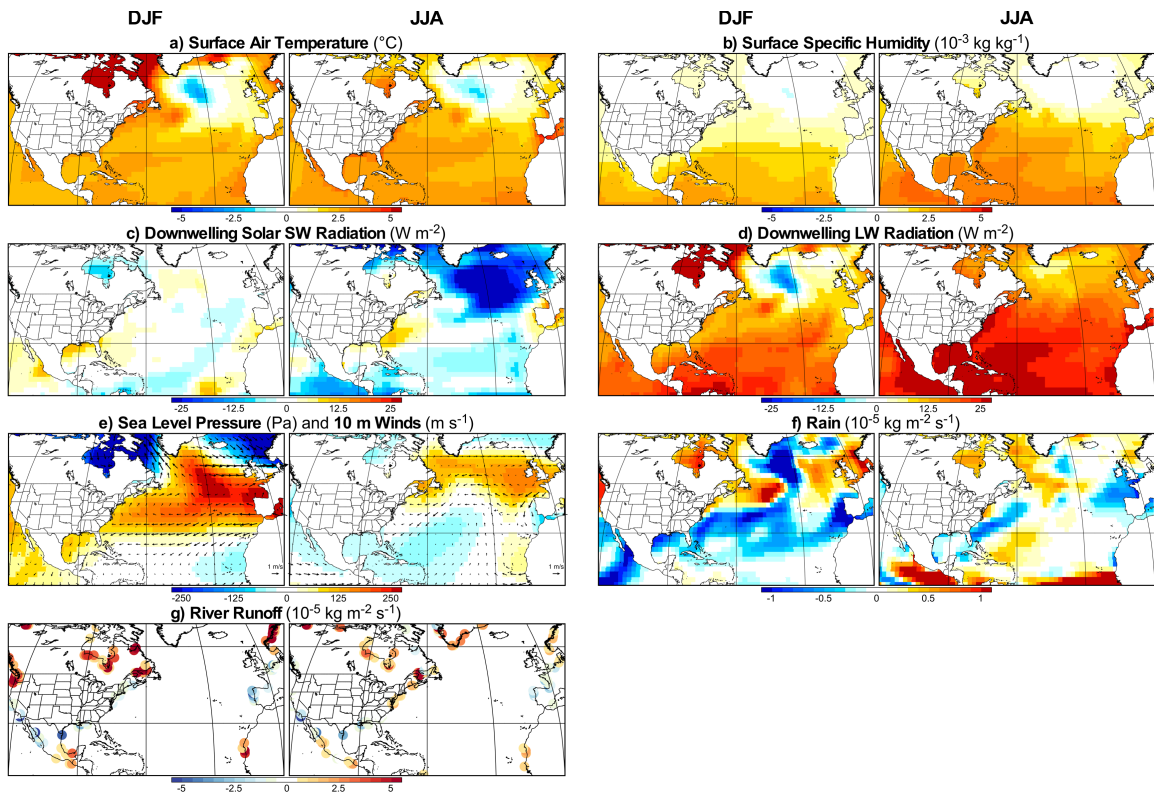


37

38 **Fig. 5.** (top) Maps of DJF GFDL-ESM2M responses of ocean bottom temperature to
39 RCP 8.5 radiative forcing changes, estimated as the mean differences between
40 two time periods representing future (yrs. 2070-2099) and present-day (yrs.
41 1976-2007) climate conditions. (bottom) The same as the top but for the JJA.

42

43

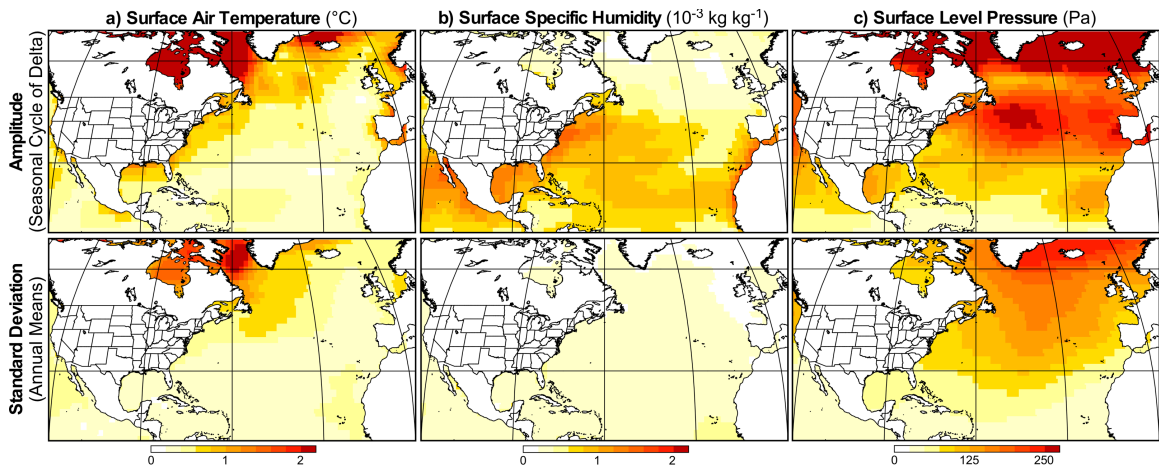


44

45 **Fig. 6.** Maps of DJF and JJA GFDL-ESM2M responses of a) surface air temperature,
 46 b) surface specific humidity, c) downwelling solar short wave radiation, d)
 47 downwelling long wave radiation, e) sea level pressure and surface (10 m)
 48 winds, f) rainfall rate, and g) river runoff to RCP 8.5 radiative forcing changes,
 49 estimated as the mean differences between two time periods representing future
 50 (yrs. 2070-2099) and present-day (yrs. 1976-2007) climate conditions.

51

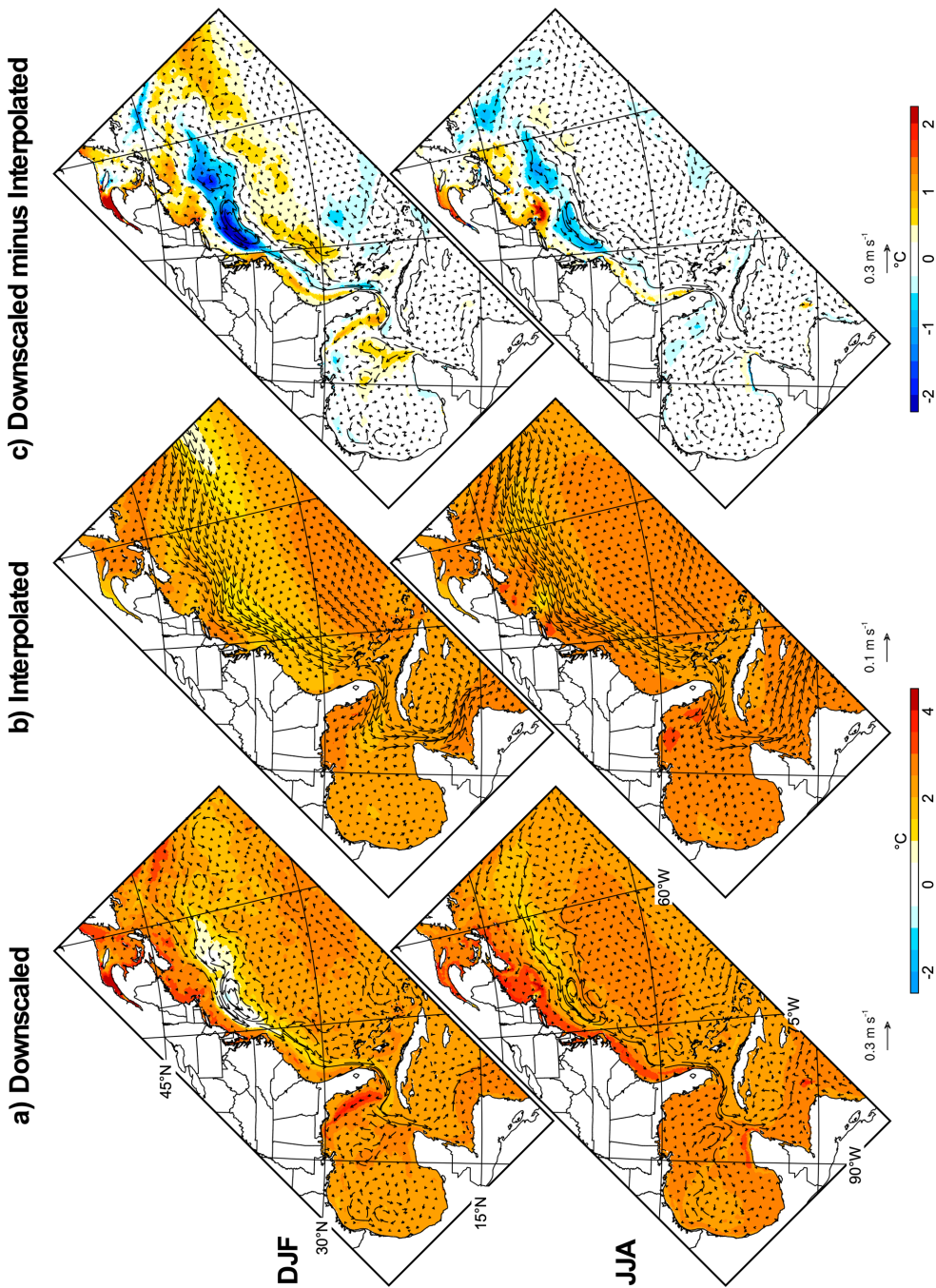
52



53

54 **Fig. 7.** (top) Maps of the amplitude of seasonal cycle of delta for a) surface air
 55 temperature, b) surface specific humidity, and c) sea level pressure, where the
 56 amplitude is defined as a half of the difference between the maximum and
 57 minimum of monthly delta. (bottom) The standard deviation of annual means of
 58 corresponding fields during yrs. 1976-2005 derived from CORE version 2 data
 59 set (Large and Yeager 2009).

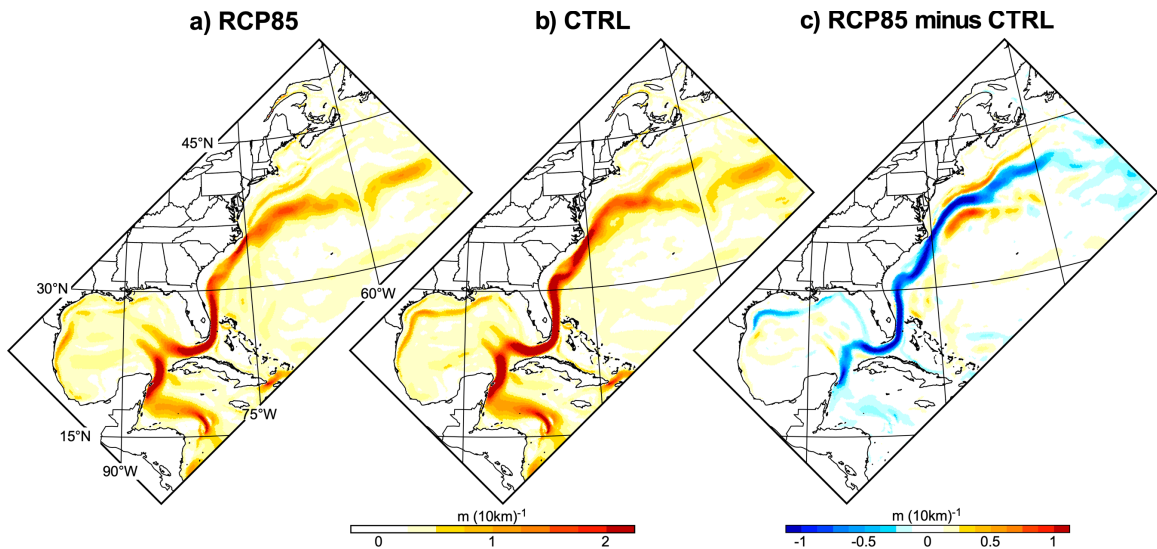
60



61

62 **Fig. 8.** (top) Maps of projected DJF sea surface temperature (color shadings) and
 63 surface current (vectors) responses, derived from a) ROMS downscaling and b)
 64 GFDL ESM2M simulations. For the ease of comparisons, the GFDL ESM2M
 65 responses were bilinearly interpolated to the ROMS grid, and the differences, a)
 66 minus b), are shown in c). (bottom) The same as the top but for the JJA.

67

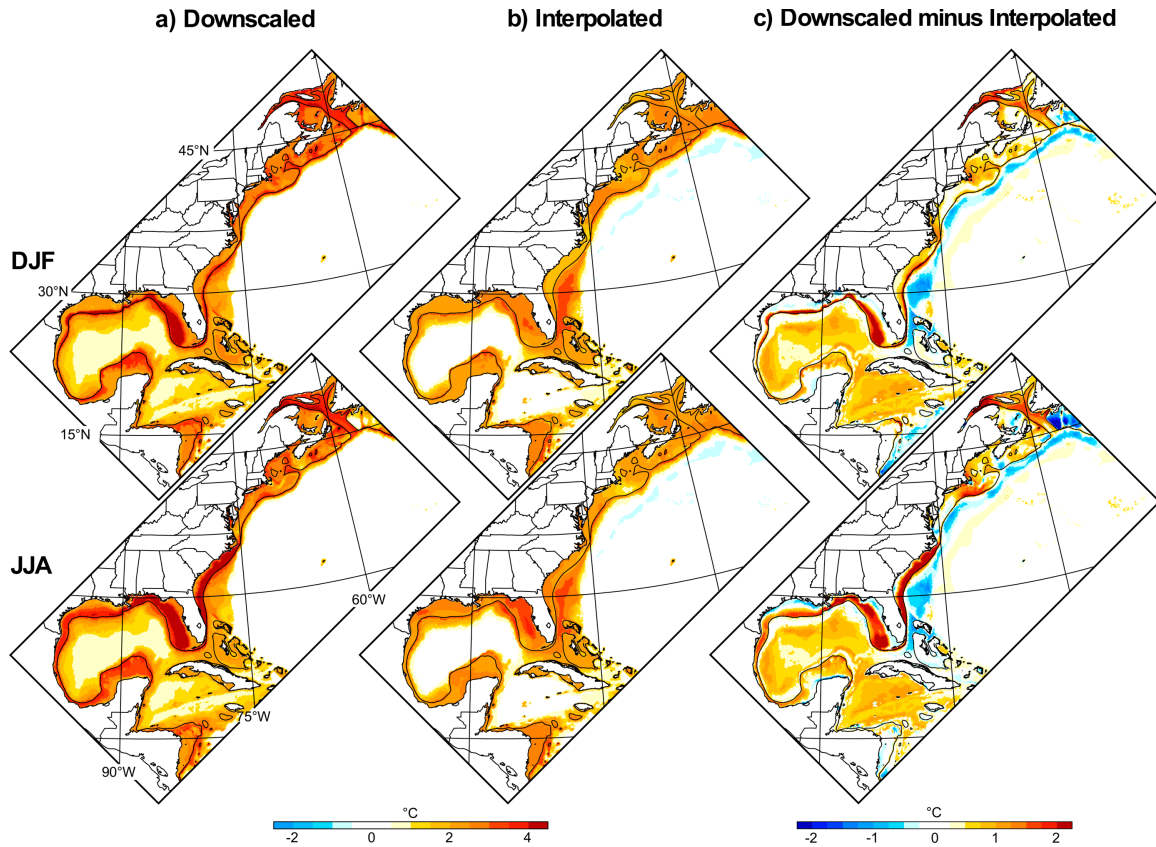


68

69 **Fig. 9.** Maps of horizontal gradient magnitude ($\sqrt{(\partial \bar{\eta} / \partial x)^2 + (\partial \bar{\eta} / \partial y)^2}$) of annually
 70 averaged sea surface height derived from a) RCP85 and b) CTRL simulations.
 71 The differences, a) minus b), are shown in c).

72

73

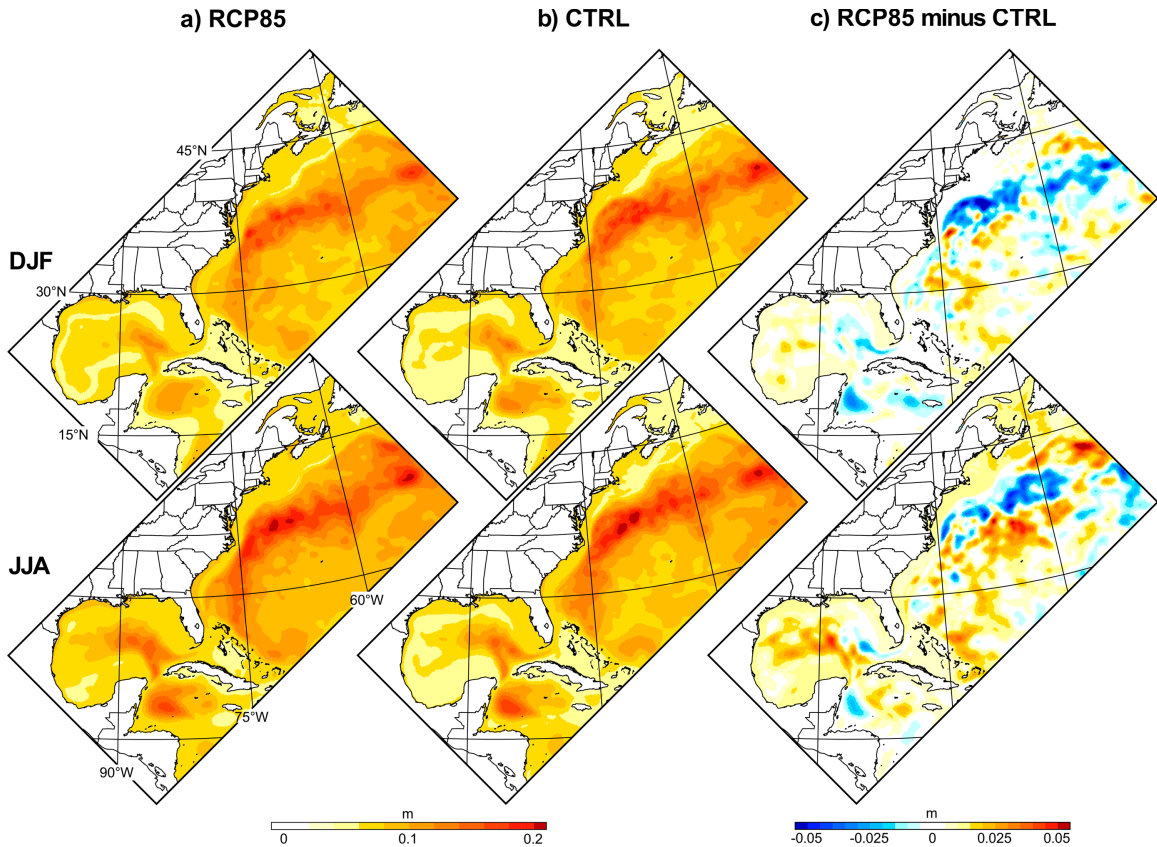


74

75 **Fig. 10.** (top) Maps of projected DJF ocean bottom temperature responses, derived from
 76 a) ROMS downscaling and b) GFDL ESM2M simulations. For the ease of
 77 comparisons, the GFDL ESM2M responses were bilinearly interpolated to the
 78 ROMS grid, and the differences, a) minus b), are shown in c). The grey
 79 contours in each map represent 200 m isobath. (bottom) The same as the top but
 80 for the JJA.

81

82

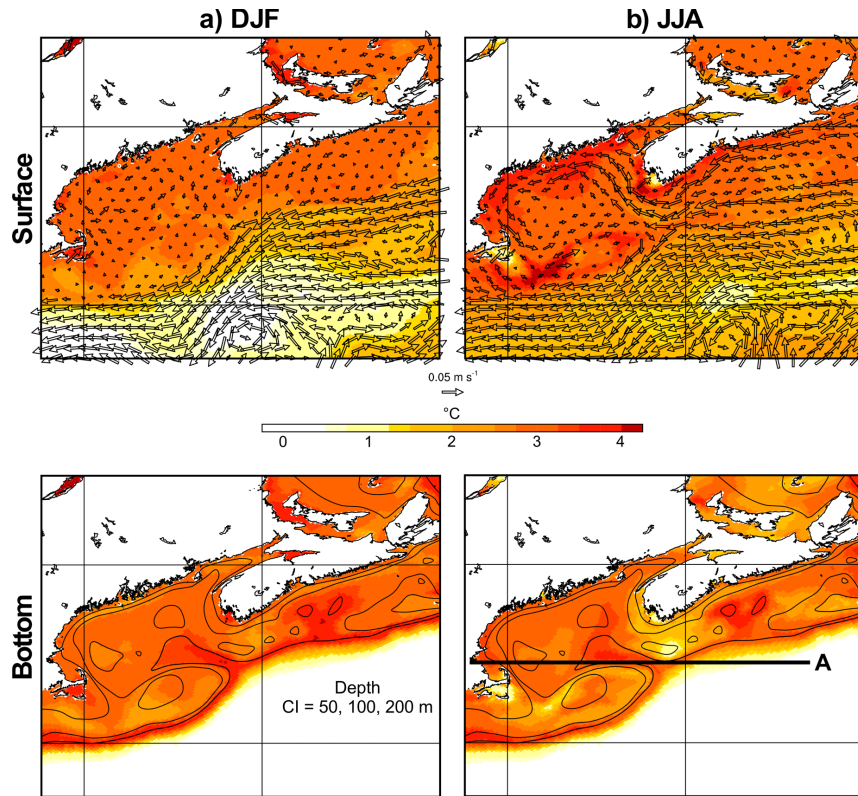


83

84 **Fig. 11.** (top) Maps of DJF high pass filtered transient ocean eddy statistics derived as
 85 sea surface height variance, $\bar{\eta}'^{1/2}$, in a) RCP85 and b) CTRL simulations. The
 86 differences, a) minus b), are shown in c). See text for the details of ocean eddy
 87 statistics estimation. (bottom) The same as the top but for the JJA.

88

89

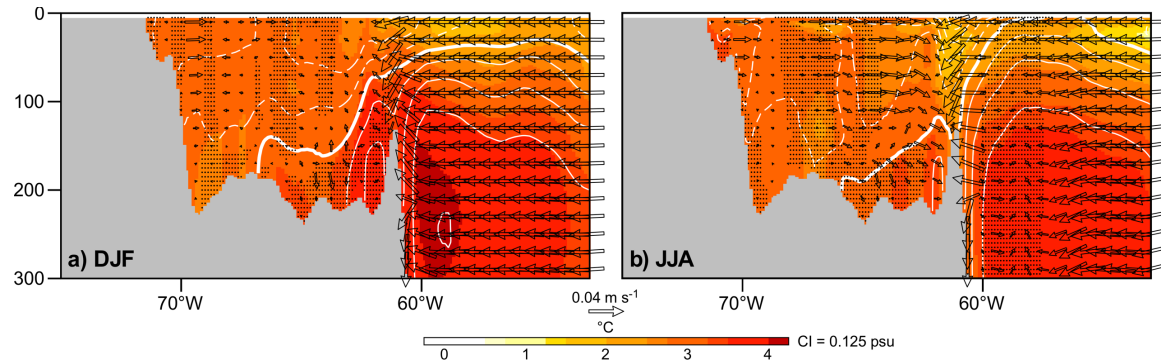


90

91 **Fig. 12.** (top) Maps of projected a) DJF and b) JJA temperature (color shadings) and
 92 current (vectors) responses at surface derived from ROMS downscaling
 93 exercise. (bottom) The same as the top but for the responses at ocean bottom.
 94 The thick black line A in the bottom panel represents the zonal cross section
 95 (42°N latitude) used in Fig. 13.

96

97



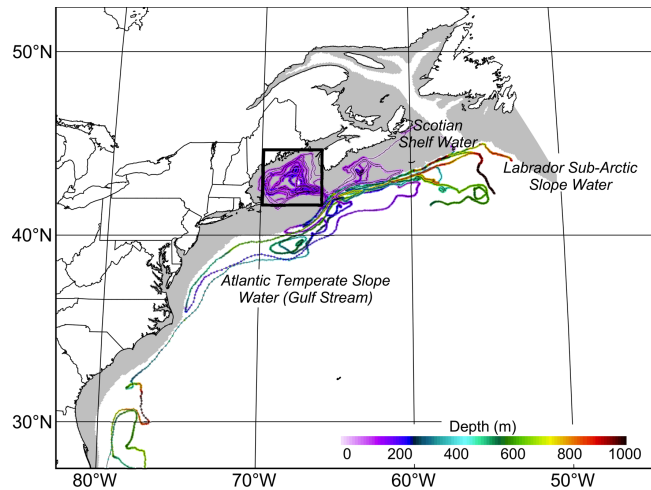
98

99 **Fig. 13.** Zonal cross section of projected a) DJF and b) JJA temperature (color
100 shadings), salinity (white contours), and zonal and vertical current (vectors)
101 responses derived from ROMS downscaling runs along the line A (see Fig. 12).
102 The anomalous northward meridional velocities are striped. Negative (zero)
103 salinity changes are denoted as dashed (thick) white contours.

104

105

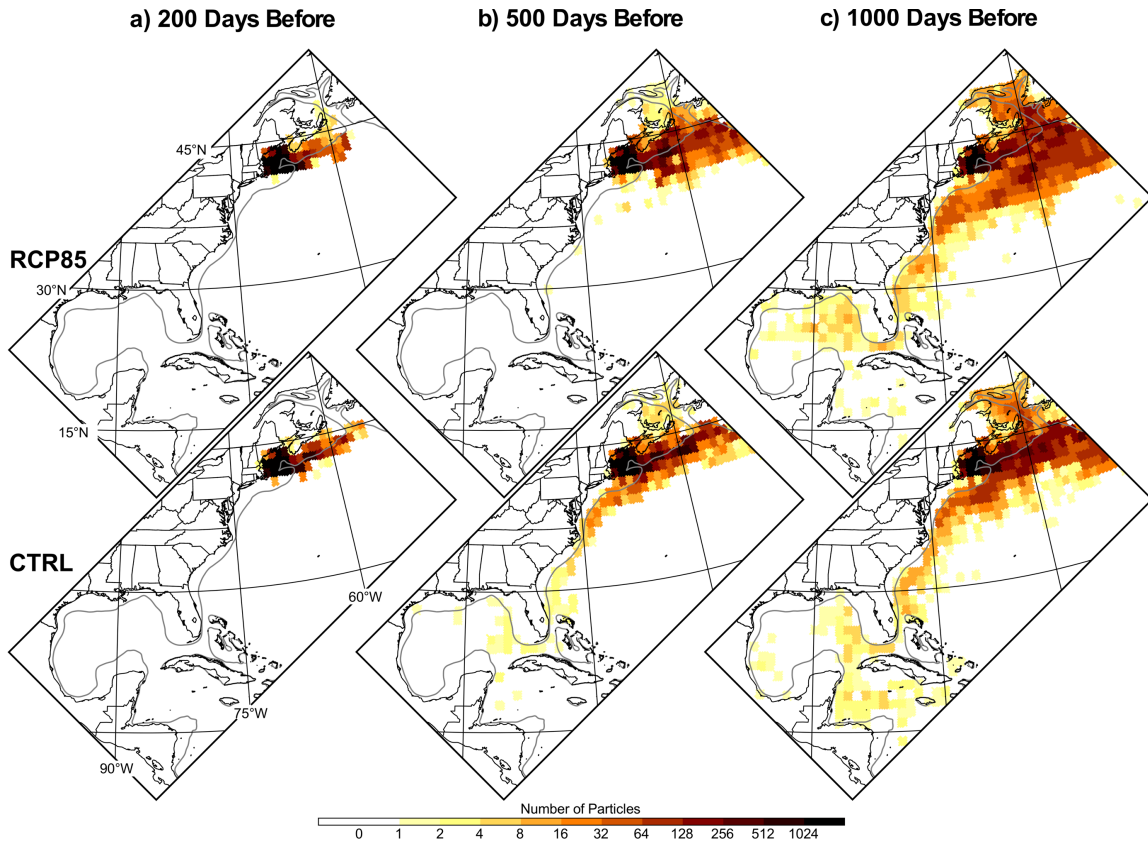
106



113

107 **Fig. 14.** The initial location map of 28,899 particles. The location is denoted as thick
108 black box representing the volumes spanning 41.63-44.61°N, 69.90-65.96°W,
109 and 145-327 m. The colored lines denote the three-dimensional backward
110 tracking of randomly chosen 20 particles located initially within the box for
111 1,000 days. The grey shadings in each map represent the continental shelves
112 where the water depth is shallower than 200 m.

114

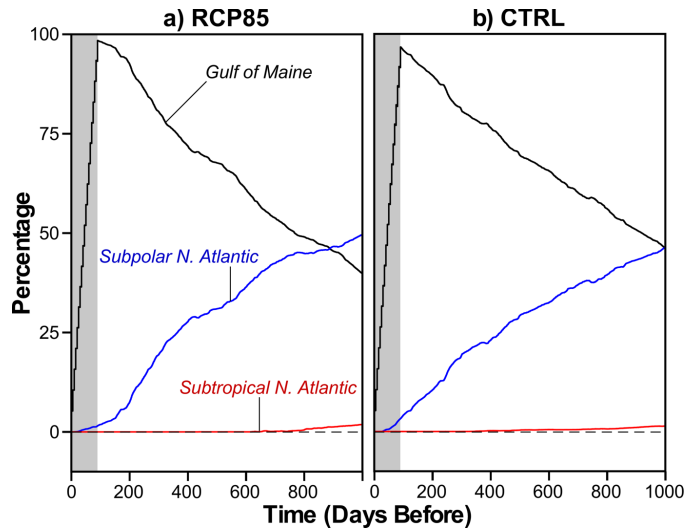


115

116 **Fig. 15.** (top) Maps of particle density at a) 200, b) 500, and c) 1,000 days before the
 117 initial time (June 2nd) derived from RCP85 run. (bottom) The same as the top
 118 but for the CTRL. See text for the details of backward particle tracking and
 119 particle density estimation. The grey contours in each map represent 200 m
 120 isobath.

121

122



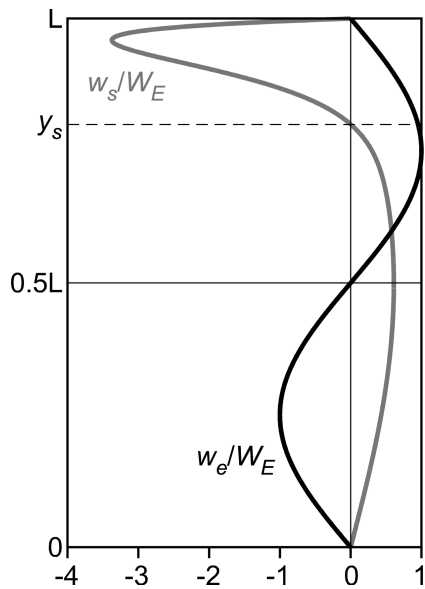
123

124 **Fig. 16.** a) Percentage changes of particle densities over time, integrated over the Gulf
125 of Maine (black line), subtropical N. Atlantic (red line), and subpolar N.
126 Atlantic (blue line), derived from the RCP85 run. b) The same as a) but for the
127 CTRL.

128

129

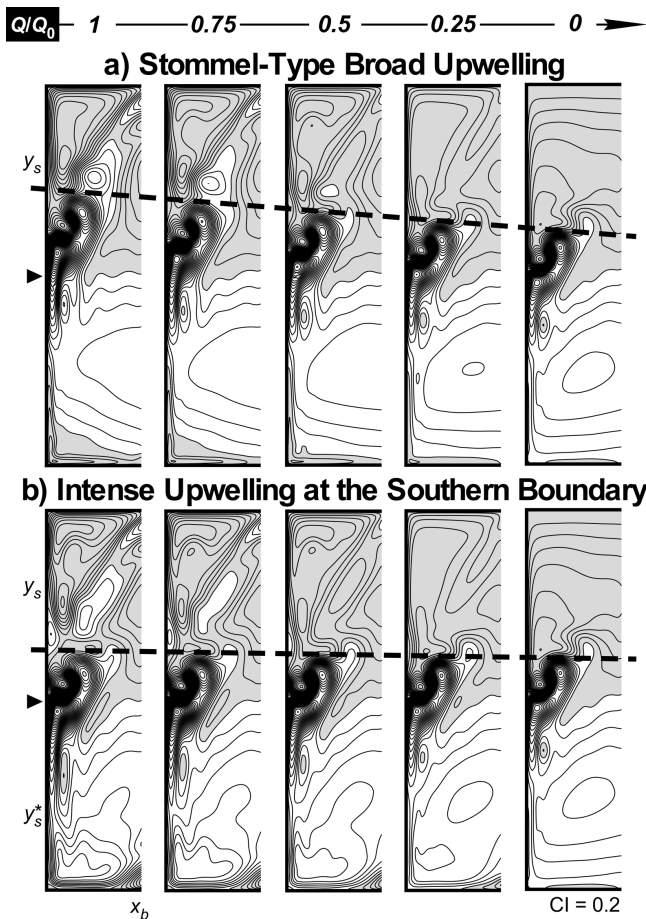
130



131 **Fig. A1.** Black and gray lines represent the meridional distributions of Ekman pumping
 132 velocity w_e at the mid-axis of the basin ($x = 0.5L$) and buoyancy flux w_s ,
 133 respectively. Both w_e and w_s are normalized by the Ekman pumping velocity
 134 W_E that yields a maximum interior Sverdrup transport of 30 Sv.

135

136



137

138 **Fig. A2.** The wind and buoyancy-driven barotropic streamfunction over the slope as the
 139 function of AMOC strength (Q ; $Q_0 = 7.5$ Sv) for the case of (a) Stommel-type
 140 broad upwelling ($0 \leq y \leq y_s$) and (b) intense upwelling at the southern boundary
 141 ($0 \leq y \leq y_s^*$). Thick black dashed lines in (a-b) denote the meridional extent of
 142 western boundary current and its extension over the slope. The contour interval
 143 is 0.2, normalized by the maximum interior Sverdrup transport. The negative
 144 values are shaded gray. The black triangles indicate the boundary current
 145 separation point at the western boundary for the case of purely wind-driven in
 146 the absence of slope.

147